# Employing three-blade propeller lanthanide complexes as molecular luminescent thermometers: study of the temperature sensing through a concerted experimental/theory approach

Dmitry M. Lyubov,[a,b] Albano N. Carneiro Neto,*[c] Ahmad Fayoumi,[a] Konstantin A. Lyssenko,[b,d] Vladislav M. Korshunov,[e] Ilya V. Taydakov,[b,e] Fabrice Salles,[f] Yannick Guari,[f] Joulia Larionova,[f] Luis D. Carlos,[c] Jérôme Long,*[f,g] Alexander A. Trifonov*[a]

*a. Institute of Organometallic Chemistry of Russian Academy of Sciences, 49 Tropinina str., GSP-445, 630950, Nizhny Novgorod, Russia.*
*b. Institute of Organoelement Compounds of Russian Academy of Sciences, 28 Vavilova str., 119334 , Moscow, Russia.*
*c. Department of Physics and CICECO – Aveiro Institute of Materials, University of Aveiro, 3810-193, Aveiro, Portugal*
*d. Lomonosov Moscow State Univ, Dept. Chem, Leninskie Gory 1, Build 3, Moscow 119991, Russia.*
*e. P. N. Lebedev Physical Institute of the Russian Academy of Sciences, Leninskiy Prospect 53, 119991, Moscow, Russia*
*f. ICGM, Univ. Montpellier, CNRS, ENSCM, Montpellier, France.*
*g. Institut Universitaire de France (IUF), 1 rue Descartes, 75231 Paris Cedex 05, France.*

## Contents

## S1. Additional data

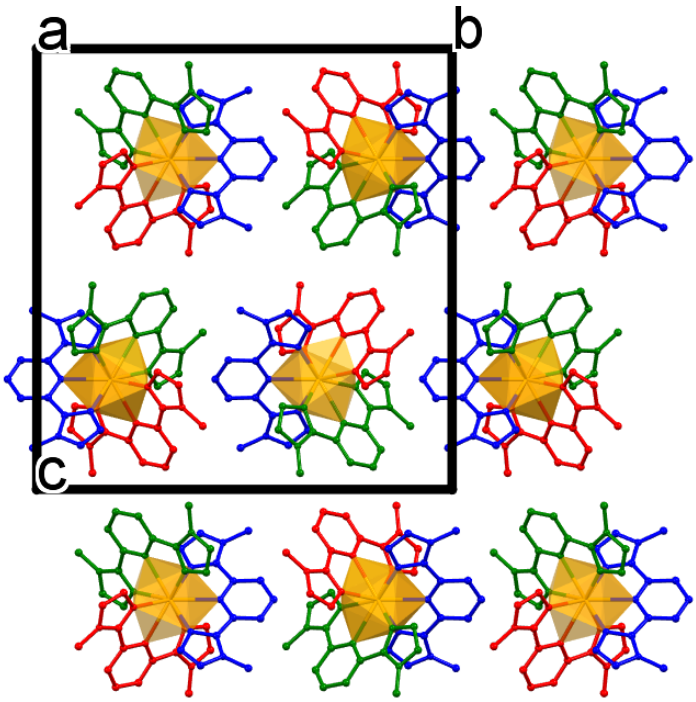


**Figure S 1**. Perspective view of the crystal packing for compounds **3** along the *a* crystallographic axis showing the two Δ and Λ enantiomers. Hydrogen, perchlorate, and solvents molecules have been omitted for clarity.

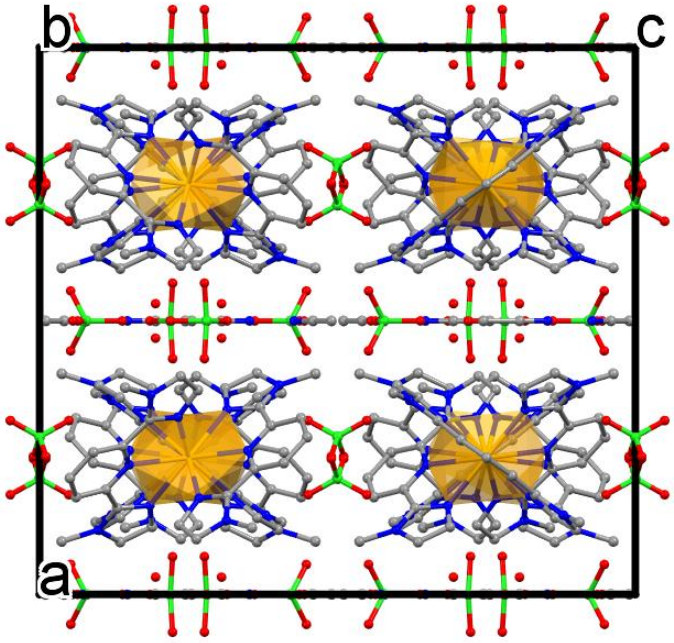


**Figure S 2**. Perspective view of the crystal packing for compounds **3** along the *b* crystallographic axis. Hydrogen atoms have been omitted for clarity.

**Table S 1**. Crystallographic data and structure refinement details for **1–5**.

| Compound | **1** | **2** | **3** | **4** | **5** |
|---|---|---|---|---|---|
| Empirical formula | $C_{43}H_{47}Cl_3EuN_{17}O_{13}$ | $C_{43}H_{47}Cl_3N_{17}O_{13}Tb$ | $C_{43}H_{47}Cl_3DyN_{17}O_{13}$ | $C_{43}H_{47}Cl_3ErN_{17}O_{13}$ | $C_{43}H_{47}Cl_3N_{17}O_{13}Yb$ |
| Formula weight | 1268.28 | 1275.24 | 1278.82 | 1283.58 | 1289.36 |
| *T*, K | 120 | 120 | 120 | 120 | 120 |
| Crystal system | Orthorhombic | Orthorhombic | Orthorhombic | Orthorhombic | Orthorhombic |
| Space group | *Cmca* | *Cmca* | *Cmca* | *Cmca* | *Cmca* |
| *a*, Å | 20.9145(14) | 20.8878(4) | 20.8878(4) | 20.9668(4) | 21.0313(12) |
| *b*, Å | 21.4762(11) | 21.4260(4) | 21.4260(4) | 21.3554(4) | 21.2857(12) |
| *c*, Å | 22.7944(12) | 22.7165(5) | 22.7165(5) | 22.6800(5) | 22.6301(12) |
| *α*, deg | 90 | 90 | 90 | 90 | 90 |
| *β*, deg | 90 | 90 | 90 | 90 | 90 |
| *γ*, deg | 90 | 90 | 90 | 90 | 90 |
| *V*, Å$^3$ | 10238.4(10) | 10166.6(4) | 10166.6(4) | 10155.1(4) | 10130.7(10) |
| *Z* | 8 | 8 | 8 | 8 | 8 |
| $d_{calcd}$, g/cm$^3$ | 1.646 | 1.666 | 1.671 | 1.679 | 1.691 |
| Absorption coefficient, mm$^{-1}$ | 14.62 | 16.3 | 17.09 | 18.92 | 20.86 |
| $F_{000}$ | 5136 | 5152 | 5160 | 5176 | 5192 |
| Crystal size, mm | 0.390×0.21×0.21 | 0.455×0.421×0.335 | 0.485×0.401×0.345 | 0.285×0.228×0.204 | 0.35 × 0.27 × 0.24 |
| θ range for data collection, deg | 1.896–28.994 | 1.901–28.997 | 1.630–28.997 | 2.108–28.999 | 1.937–27.498 |
| Reflections collected | 53374 | 78532 | 67068 | 40696 | 33773 |
| Unique / observed ($I > 2\sigma(I)$) reflections | 6987/5158 | 6931/ 4988 | 6939/5308 | 6921/4706 | 5984/3241 |
| $R_{int}$ | 0.0273 | 0.0265 | 0.0484 | 0.0527 | 0.1123 |
| Completeness to *θ*, % | 99.8 | 99.8 | 100 | 99.8 | 99.8 |
| Data / restraints / parameters | 6987/381/48 | 6931/381/48 | 6939/381/36 | 6921/381/36 | 5984/381/36 |
| $S(F^2)$ | 1.055 | 1.068 | 1.067 | 0.966 | 1.007 |
| Final *R* indices ($F^2 > 2\sigma(F^2)$) | $R_1$ = 0.0409<br>$wR_2$ = 0.1100 | $R_1$ = 0.0406<br>$wR_2$ = 0.1101 | $R_1$ = 0.0435<br>$wR_2$ = 0.1180 | $R_1$ = 0.0402<br>$wR_2$ = 0.1058 | $R_1$ = 0.0598<br>$wR_2$ = 0.14070 |
| *R* indices (all data) | $R_1$ = 0.0592<br>$wR_2$ = 0.1205 | $R_1$ = 0.0611<br>$wR_2$ = 0.1210 | $R_1$ = 0.0561<br>$wR_2$ = 0.1260 | $R_1$ = 0.0604<br>$wR_2$ = 0.1164 | $R_1$ = 0.1286<br>$wR_2$ = 0.1780 |
| Largest diff. peak and hole, e/Å$^3$ | 2.367/-1.333 | 2.457/-1.112 | 1.973/-1.922 | 1.763/-1.115 | 1.534/-1.435 |

**Table S 2**. Shape analysis for complexes **1-5**.

| | **EP** | **OPY** | **HBPY** | **JTC** | **JCCU** | **CCU** | **JCSAPR** | **CSAPR** | **JTCTPR** | **TCTPR** | **JTDIC** | **HH** | **MFF** |
|---|---|---|---|---|---|---|---|---|---|---|---|---|---|
| **1** | 31.849 | 24.319 | 18.106 | 12.916 | 9.776 | 8.771 | 2.470 | 1.692 | 1.576 | 1.555 | 12.287 | 11.720 | 2.260 |
| **2** | 31.899 | 24.259 | 18.253 | 12.962 | 9.888 | 8.879 | 2.395 | 1.648 | 1.488 | 1.505 | 12.453 | 11.755 | 2.226 |
| **3** | 32.096 | 24.242 | 18.288 | 13.088 | 9.937 | 8.892 | 2.344 | 1.573 | 1.458 | 1.416 | 12.477 | 11.828 | 2.153 |
| **4** | 32.338 | 24.326 | 18.470 | 13.245 | 10.010 | 9.068 | 2.273 | 1.489 | 1.420 | 1.313 | 12.529 | 11.855 | 2.072 |
| **5** | 32.284 | 24.293 | 18.616 | 13.258 | 10.042 | 9.129 | 2.238 | 1.474 | 1.373 | 1.299 | 13.698 | 11.867 | 2.069 |

EP: Enneagon
OPY: Octagonal pyramid
HBPY: Heptagonal bipyramid
JTC: Johnson triangular cupola J3
JCCU: Capped cube J8
CCU: Spherical-relaxed capped cube
JCSAPR: Capped square antiprism J10
CSAPR: Spherical capped square antiprism
JTCTP: Tricapped trigonal prism J51
TCTPR: Spherical tricapped trigonal prism
JTDIC: Tridiminished icosahedron J63
HH: Hula-hoop
MFF: Muffin

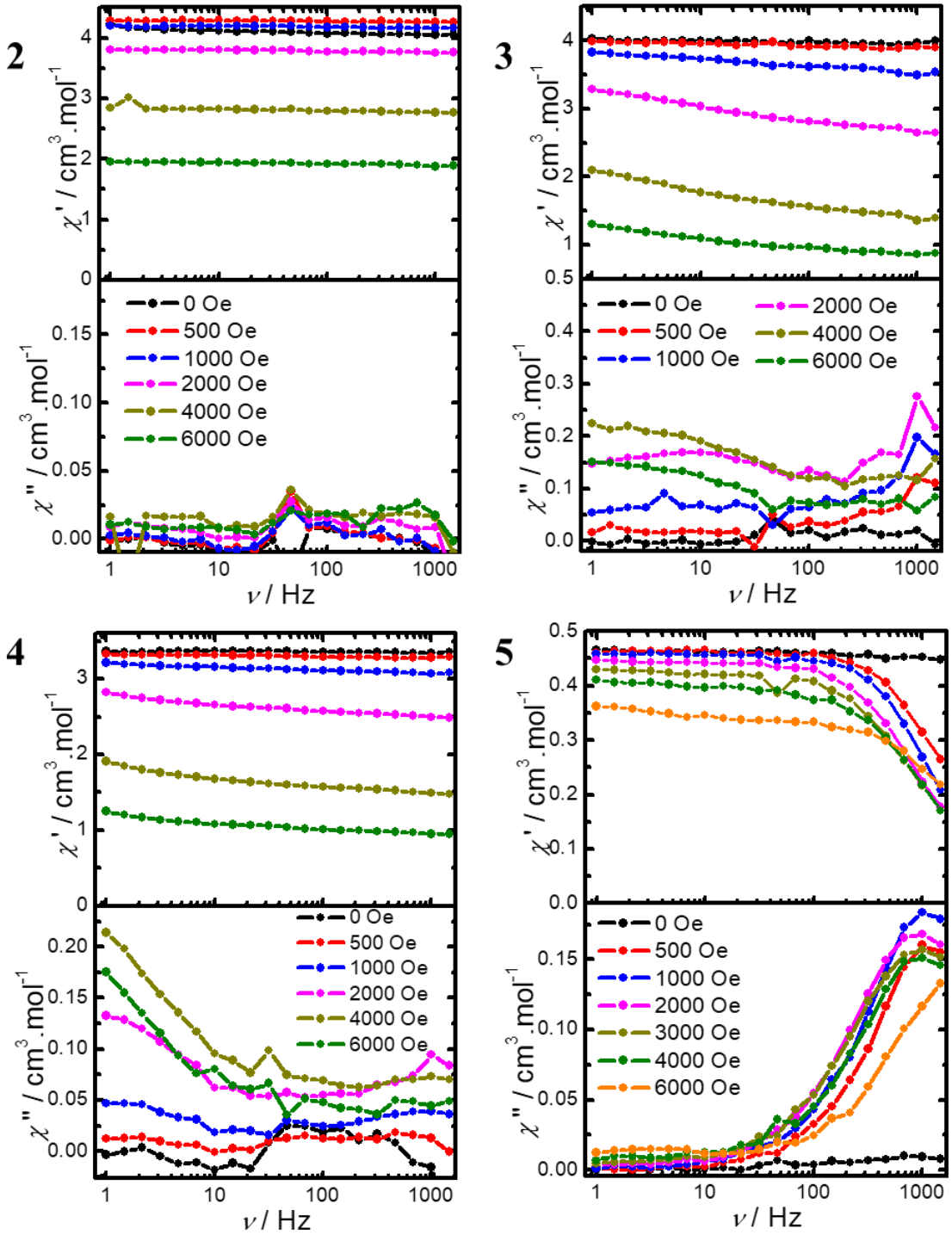


**Figure S 3**. Frequency dependence of $\chi'$ and $\chi''$ for complexes **2-5** (2 K) for various DC-fields.

**Ab initio calculations (magnetic properties)**

CASSCF calculations were performed with ORCA 5.0.2[1] using the crystallographic structures of **2-5** with hydrogen-optimized geometries. Tolerance for energy convergence is fixed at $10^{-7}$. An active space considering the seven 4f orbitals with 8 eletrons CAS (8, 7) for all septets (7 roots) for $Tb^{3+}$, 9 electrons CAS (9, 7) for all the

sextets (21 roots) for $Dy^{3+}$, 11 electrons CAS (11, 7) for all the quartets (35 roots) for $Er^{3+}$ and 13 electrons CAS (13, 7) for all the duets (7 roots) for $Yb^{3+}$ were used. The def2 Ahlrichs basis sets were used: DKH-DEF2-TZVP for all atoms, except for the Ln ions for which SARC2-DKH-QZVP basis set was employed. Indeed, relativistic effects can have a high impact when heavy atoms are involved and these effects should not be ignored. The AUTOAUX feature was used to automatically generate auxiliary basis sets within the RIJCOSX approximation to speed-up the calculations. Then, the SINGLE_ANISO[2] program implemented in ORCA was used to obtain details about the magnetic relaxation.

**Table S 3.** *Ab initio* calculated energies and *g*-tensor main values for **2-5** for the ground multiplets $J = 6$ (**2**), $J = 15/2$ (**3**), $J = 15/2$ (**4**) and $J = 7/2$ (**5**).

| | **2** | | | |
|---|---|---|---|---|
| **States** | **Energy ($cm^{-1}$)** | $g_x$ | $g_y$ | $g_z$ |
| **1** | 0.00 | 1.966718 | 2.100836 | 3.358783 |
| **2** | 0.26 | - | - | - |
| **3** | 63.69 | - | - | - |
| **4** | 64.47 | - | - | - |
| **5** | 102.38 | - | - | - |
| **6** | 108.96 | - | - | - |
| **7** | 146.50 | - | - | - |
| **8** | 176.31 | - | - | - |
| **9** | 198.64 | - | - | - |
| **10** | 256.13 | - | - | - |
| **11** | 267.66 | - | - | - |
| **12** | 299.65 | - | - | - |
| **13** | 304.41 | - | - | - |
| | **3** | | | |
| **KD** | **Energy ($cm^{-1}$)** | $g_x$ | $g_y$ | $g_z$ |
| **1** | 0.00 | 0.04348458 | 0.06735437 | 19.53751710 |
| **2** | 92.692 | 0.46976226 | 1.06076333 | 16.40301549 |
| **3** | 140.093 | 4.26066250 | 6.70488223 | 6.70488223 |
| **4** | 180.808 | 0.41805148 | 2.71331742 | 11.14954768 |
| **5** | 237.066 | 0.26491273 | 2.07214473 | 13.87399642 |
| **6** | 274.316 | 0.17741312 | 4.59032702 | 13.31982440 |
| **7** | 300.926 | 0.73318686 | 3.92691475 | 11.79602408 |
| **8** | 354.532 | 0.26936954 | 1.49032042 | 17.70518995 |
| | **4** | | | |
| **KD** | **Energy ($cm^{-1}$)** | $g_x$ | $g_y$ | $g_z$ |
| **1** | 0.00 | 1.76063680 | 4.30025604 | 12.15450762 |
| **2** | 30.494 | 6.3147085 | 5.02797513 | 2.47716750 |
| **3** | 85.763 | 1.01466718 | 4.60982140 | 10.78943053 |
| **4** | 121.994 | 0.98218145 | 3.09924229 | 9.2469922 |
| **5** | 188.581 | 2.04516509 | 4.67853390 | 9.10965465 |
| **6** | 224.710 | 0.88265353 | 3.45775676 | 7.33700617 |
| **7** | 254.823 | 1.28702766 | 2.09242436 | 8.29385289 |
| **8** | 314.190 | 2.28820858 | 2.95417245 | 13.34280903 |
| | **5** | | | |
| **KD** | **Energy ($cm^{-1}$)** | $g_x$ | $g_y$ | $g_z$ |
| **1** | 0.00 | 0.95018111 | 2.83921267 | 5.61975755 |
| **2** | 86.753 | 3.28690240 | 2.41512262 | 0.16391664 |
| **3** | 200.279 | 0.09283511 | 1.89509038 | 5.36310038 |
| **4** | 311.743 | 1.16638782 | 1.22360587 | 7.13800281 |

The absence of slow-relaxation of the magnetization could be rationalized by simple electrostatic considerations. Among the lanthanide ions used in this series, $Tb^{3+}$ is the only non-Kramers ion ($^7F_6$ ground state). Hence, the occurrence of slow relaxation of the magnetization requires a particular high symmetry. In contrast, $Dy^{3+}$, $Er^{3+,}$ and $Yb^{3+}$ are all Kramers ions with doubly degenerate ground states. This may provide the possibility of slow relaxation of the magnetization, not strictly axial or high symmetry complexes. However, the lanthanide ions show different angular dependence of their 4*f* electronic density: $Dy^{3+}$ presents an oblate electronic density requiring an axial crystal-field to enhance its anisotropy while $Er^{3+}$ has a prolate one that necessitates an equatorial crystal-field. The $Yb^{3+}$ could exhibit either a prolate or oblate electronic density depending on the nature of the ground doublet. The magnetic results clearly show that the symmetry and crystal-field observed in the three-blade propeller complexes is not sufficient to induce a strong magnetic anisotropy.

*Ab initio* calculations at the CASSCF levels reveals the presence of low -first excited state associated with non-negligible transverse components ($g_x$ and $g_y$) of the *g* tensor for the ground state (Table S 3). This lack of axiality explains the observed QTM.

To further rationalize this, the orientation of the anisotropic axes of the ground Kramers doublet of the dysprosium analogue **3** is found to be almost collinear (deviation of 7.1°) to one of the $Dy{-}N_{imidazpme}$ bonds (Figure S4). However, the absence of negative charge brought by the L ligand as well as long Dy−N distances does not provide an axial crystal-field necessary to observe a slow relaxation of the magnetization. Similarly, the coordination environment could not induce an equatorial crystal-field suitable for prolate ions.

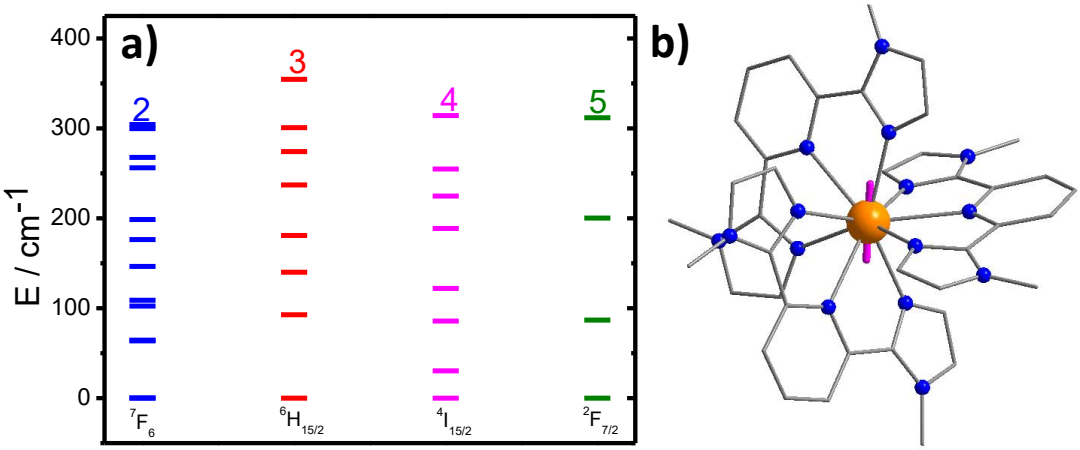


**Figure S 4**. a) Crystal-field splitting obtained from CASSCF calculations for **2-5**; b) Orientation of the anisotropic axis (purple) in **3** obtained from *ab initio* calculations.

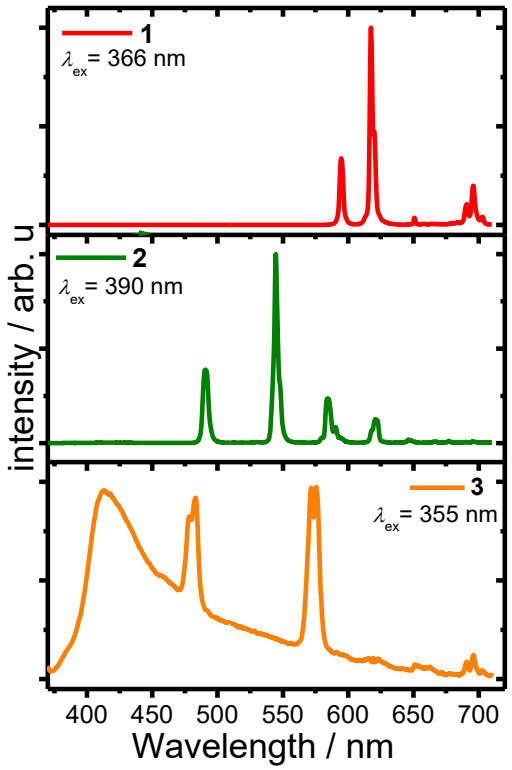


**Figure S 5**. Full-range room temperature emission spectra for **1**, **2** and **3**.

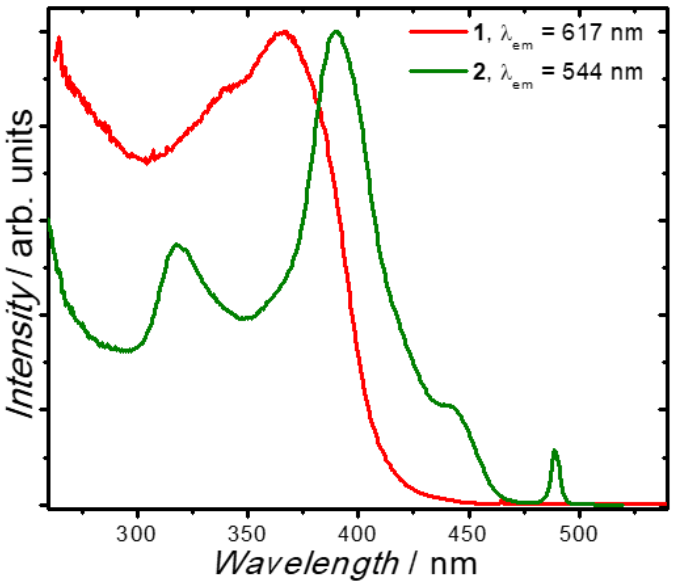


**Figure S 6**. Room temperature excitation spectra for **1** and **2**.

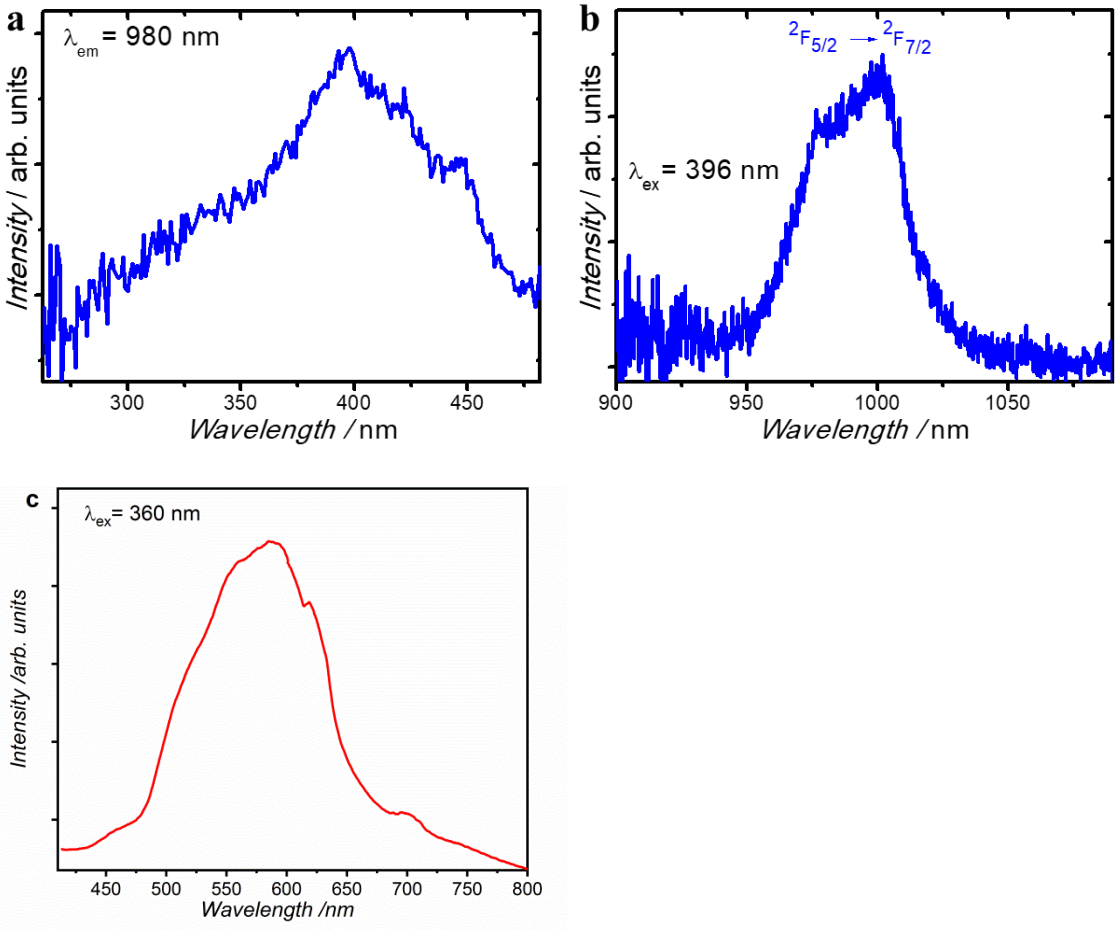


**Figure S 7**. a) Excitation and b) emission spectra of ytterbium complex **5**. c) Phosphorescence spectrum of complex **6** at 77 K.

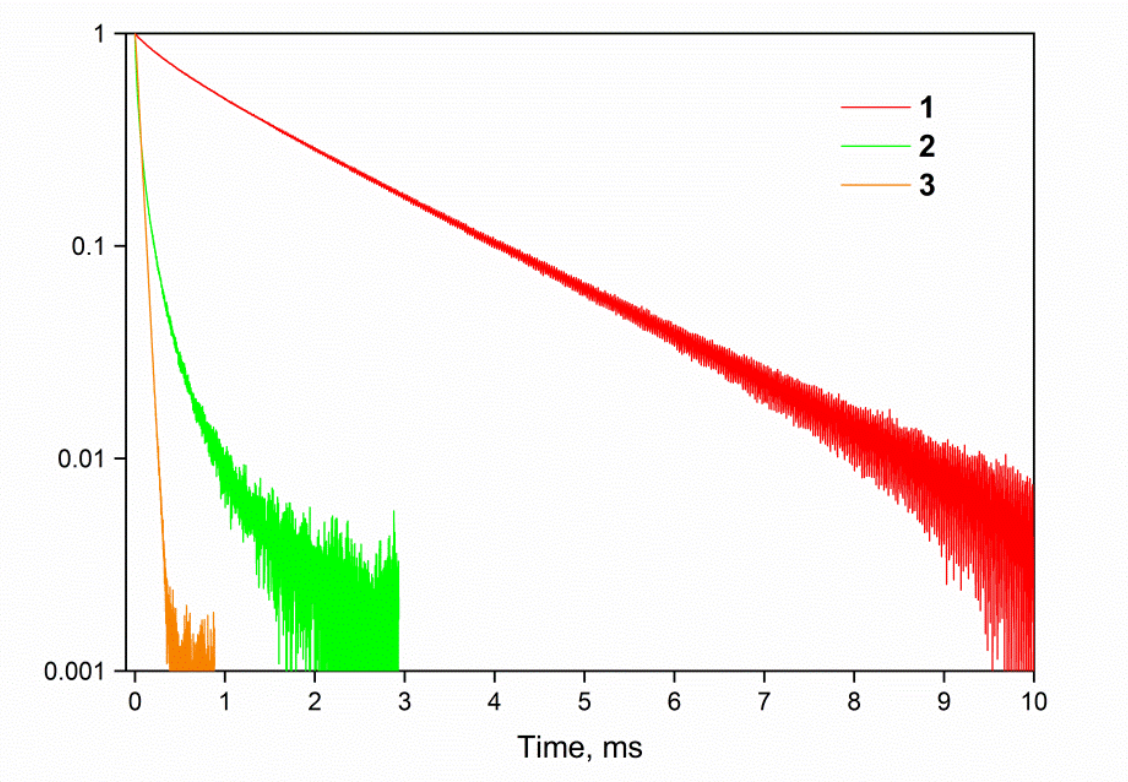


**Figure S 8**. PL decays measured for investigated compounds **1**, **2** and **3**.

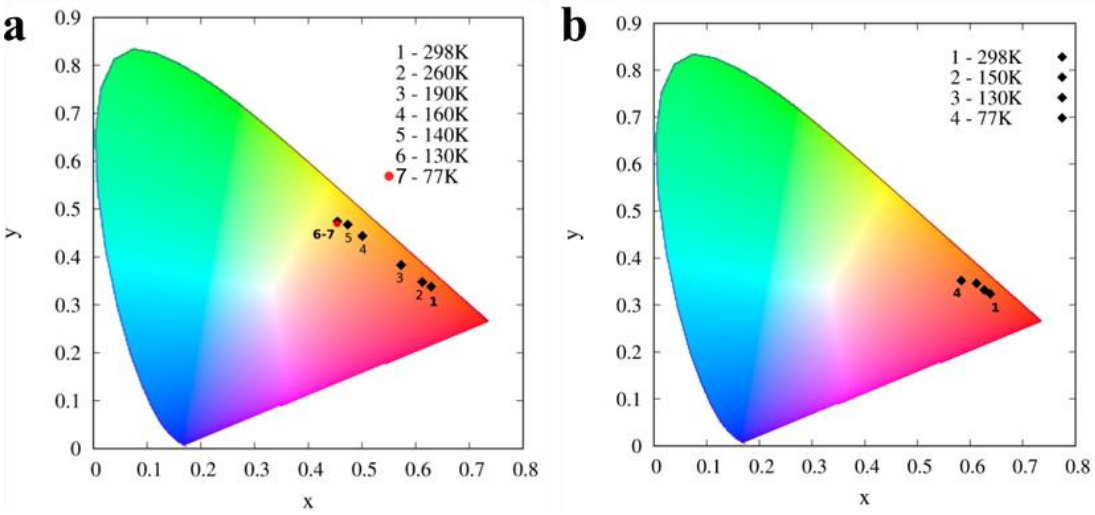


**Figure S 9**. CIE coordinates for Eu-Tb mixed complex a) $[Eu_{0.50}Tb_{0.50}L_3](ClO_4)_3 \cdot H_2O \cdot 2MeCN$ and b) $[Eu_{0.17}Tb_{0.83}L_3](ClO_4)_3 \cdot H_2O \cdot 2MeCN$ at different temperatures.

**Table S 4.** Maximum relative thermal sensitivity ($S_m$) and temperature at which it occurs ($T_m$) for some $Eu^{3+}/Tb^{3+}$ complexes and $Eu^{3+}/Tb^{3+}$-doped MOFs, sorted by year.

| Material | $T_m$ (K) | $S_m$ (%K$^{-1}$) | Year | Ref. |
|---|---|---|---|---|
| MOFs | 318 | 0.3 | 2013 | [a] |
| | 300 | 3.3 | | [b] |
| | 300 | 2.8 | | |
| | 250 | 2.5 | | |
| | 275 | 2.0 | | |
| | 300 | 16 | 2014 | [c] |
| | 333 | 4.5 | | [d] |
| | 275 | 2.4 | 2015 | [e] |
| | 293 | 1.3 | | [f] |
| | 293 | 0.3 | | [g] |
| | 300 | 0.1 | | [h] |
| | 300 | 0.2 | | |
| | 300 | 0.2 | | |
| | 328 | 1.4 | | |
| | 250 | 4.9 | 2016 | [i] |
| | 293 | 3.8 | | [j] |
| | 350 | 0.3 | 2017 | [l] |
| | 319 | 1.7 | | [k] |
| | 319 | 1.3 | | |
| | 313 | 0.7 | | [m] |
| | 340 | 1.4 | 2018 | [n] |
| | 303 | 1.2 | | [o] |
| | 310 | 9.4 | 2019 | [p] |
| | 300 | 0.2 | 2020 | [q] |
| | 338 | 0.2 | 2021 | [r] |
| | 333 | 0.2 | | |
| | 314 | 0.2 | | |
| | 284 | 0.3 | | |
| | 251 | 0.4 | | |
| Complexes | 296 | 5.8 | 2015 | [s] |
| | 293 | 1.5 | 2016 | [t] |
| | 293 | 7.1 | 2017 | [u] |
| | 262 | 2.0 | 2021 | [v] |
| | 290 | 2.3 | 2021 | [w] |

[a] A. Cadiau, *et al., ACS Nano* **2013**, 7, 7213-7218. [b] X. Rao, *et al., J. Am. Chem. Soc.* **2013**, 135, 15559-15564. [c] Y. J. Cui, *et al., Chem. Commun.* **2014**, 50, 719-721. [d] Y. Zhou, *et al., Chemical communications* **2014**, 50, 15235-8. [e] Y. Wei, *et al., Dalton Trans.* **2015**, 44, 3067-74. [f] Y. Cui, *et al., Adv. Mater.* **2015**, 27, 1420-1425. [g] Y. Zhou, B. Yan, *J. Mater. Chem. C* **2015**, 3, 9353-9358. [h] S. N. Zhao, *et al., Adv. Funct. Mater.* **2015**, 25, 1463-1469. [i] L.-L. Wu, *et al., Cryst. Eng. Comm.* **2016**, 18, 4268-4271. [j] W. Liu, *et al., Chem. Eur. J.* **2016**, 22, 11170-11175. [l] H. Wang, *et al., J. Solid State Chem.* **2017**, 246, 341-345. [k] T. Xia, *et al., J. Mater. Chem. C* **2017**, 5, 5044-5047. [m] D. Ananias, *et al. ,Chem. Mater.* **2017**, 29, 9547-955. [n] T. Chuasaard, *et al. ,Inorg. Chem.* **2018**, 57, 2620-2630. [o] P. Farger, *et al., Beilstein J Nanotech* **2018**, 9, 2775-2787. [p] Y. Pan, *et al., Dalton Trans.* **2019**, 48, 3723-3729. [q] G. E. Gomez, *et al., Chem. Mater.* **2020**, 32, 7458-7468. [r] V. Trannoy, *et al., Adv. Opt. Mater.* **2021**, 9, 2001938. [s] R. Piñol, *et al., ACS Nano* **2015**, 9, 3134-3142. [t] M. Rodrigues, *et al., Adv. Funct. Mater.* **2016**, 26, 200-209. [u] C. D. S. Brites, *et al., Nano Letters* **2017**, 17, 4746-4752. [v] A. N. Carneiro Neto, *et al., Adv. Opt. Mater.* **2021**, 2101870.[w] Y. Chen, *et al., Dyes and Pigment.* **2021**, 109671.

## S2. Theoretical modeling methodology for luminescence

### S2.1 In silico experiments

A DFT level of theory was employed to obtain structural and electronic properties such as ground state molecular geometry and molecular orbitals compositions of the first excited Singlet ($S_1$) and Triplet ($T_1$) states involved in the energy transfer. The molecular geometry optimization was performed applying Gaussian 09 program[3] with B3LYP functional[4,5]. The basis set 6-31G(d) was employed for hydrogen, carbon, nitrogen atoms and the $Ln^{3+}$ ion was treated with MWB52 or MWB54 ($Ln^{3+}$ = $Eu^{3+}$ or $Tb^{3+}$, respectively) basis set,[6] which includes 52 or 54 electrons in the core with its associated valence basis set for the lanthanide ion.

Figure S10a shows the superposition of the DFT optimized structure (purple spheres) with the crystal structure of the $[LnL_3]^{3+}$ complex, indicating that the calculated structure is in good agreement with the experimental structure obtained from the crystallographic data. The $Ln^{3+}$ coordination polyhedron (Figure S10b) is close to a $D_{3h}$ point group symmetry (12 symmetry elements: E, $2C_3$, $3C_2$, $\sigma_h$, $2S_3$, and $3\sigma_v$).

The root-mean-square deviations (RMSD) of atomic positions between these structures are equal to 0.131 and 0.441 Å for the coordination polyhedron and the whole structure, respectively. Due to the number of atoms involved, these values are relatively high compared with those presented in Ref. [7] (RMSD equals 0.064 Å for the coordination polyhedron and 0.147 Å for the entire structure), although, the [Ln(bbpen)Cl] is a seven-coordinate complex containing 64 atoms in its structure, while the $[LnL_3]^{3+}$ is nine-coordinate and has a total of 96 atoms. Thus, the obtained RMSD values for the $[LnL_3]^{3+}$ can be considered acceptable and there are no huge deviations in Figure S10a.

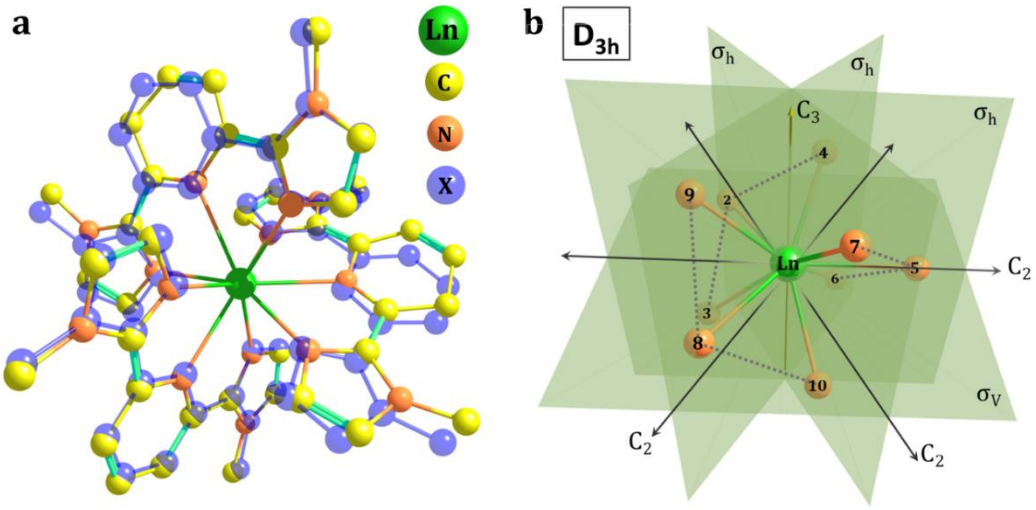


**Figure S10**. a) Superposition between optimized structure (purple spheres) and the crystallographic one (green, yellow, and orange spheres) of the $[LnL_3]^{3+}$ complex. The hydrogen atoms were omitted for clarity. b) Coordination polyhedron close to the $D_{3h}$ point group symmetry (some symmetry elements are showed). The nitrogen atoms connected represent each ligand (2,6-bis(1-methyl-imidazol-2-y1)pyridine).

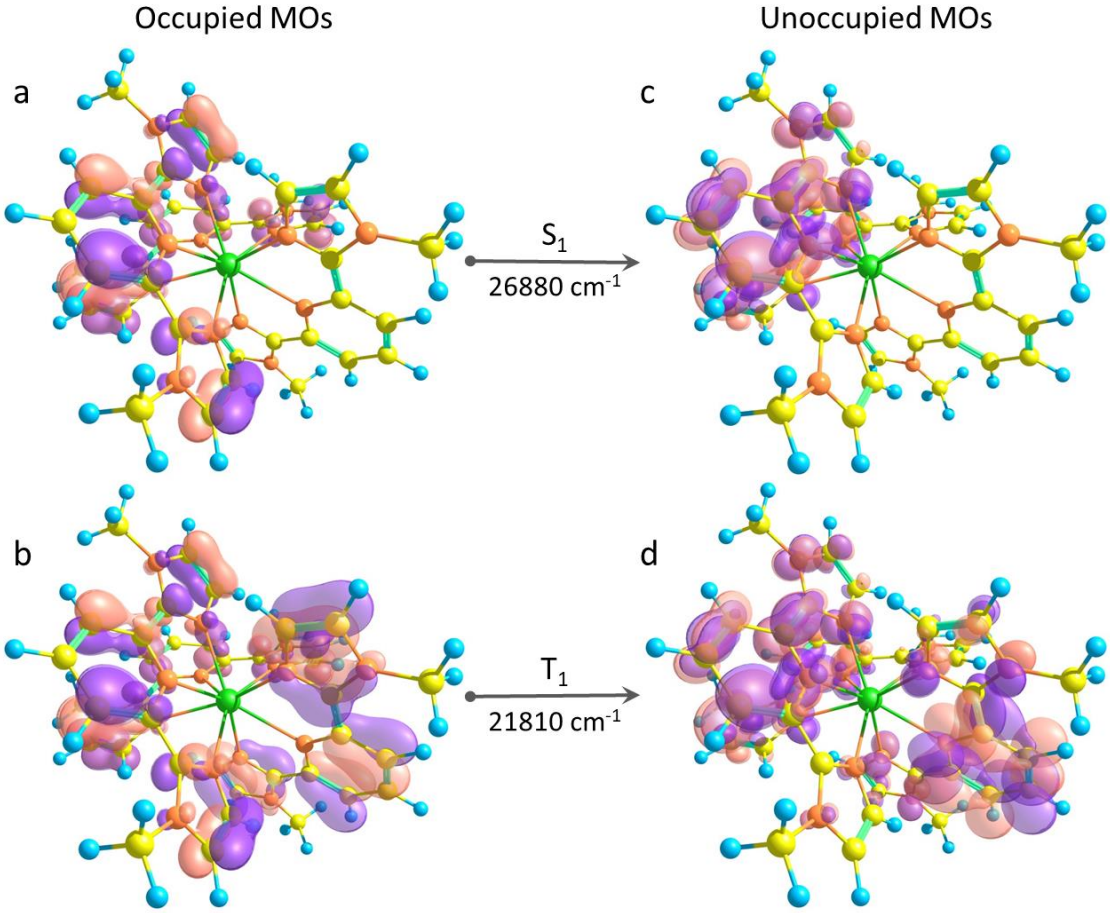


**Figure S11**. Molecular orbitals compositions for the $S_1$ and $T_1$ states. The occupied MOs (**a** and **b**) are more delocalized throughout the ligand while the unoccupied MOs (**c** and **d**) are more concentrated at the ligand's pyridine ring for both $S_1$ and $T_1$ states. Isosurfaces generated with 0.04 $e/a_0^3$.

### S2.2 Theoretical intensity parameters

The forced electric dipole (FED – Judd-Ofelt theory) and dynamic coupling (DC) are the dominant mechanisms for the 4*f*-4*f* intensities when the lanthanide occupies a non-centrosymmetric site [8–10]. The theoretical expressions here used for the intensity parameters, $\Omega_\lambda^{theo}$, have been described in detail in several references [11–13]. However, to evaluate the energy transfer through dipole-dipole mechanism (as will be detailed in next subsection), only the FED contribution should be considered.

$$\Omega_\lambda^{theo} = (2\lambda+1)\sum_{t,p}\frac{\left|B_{\lambda tp}\right|^2}{2t+1} \quad , \qquad B_{\lambda tp} = B_{\lambda tp}^{FED} + B_{\lambda tp}^{DC} \tag{S1}$$

where,

$$B_{\lambda tp}^{FED} = \frac{2}{\Delta E}\langle r^{t+1}\rangle\Theta(t,\lambda)\left(\frac{4\pi}{2t+1}\right)^{\frac{1}{2}}\sum_j \frac{e^2\rho_j g_j\left(2\beta_j\right)^{t+1}}{R_j^{t+1}}\left(Y_p^{t*}\right)_j \tag{S2}$$

$$B_{\lambda tp}^{DC} = -\left[\frac{(\lambda+1)(2\lambda+3)}{(2\lambda+1)}\right]^{\frac{1}{2}}\langle r^\lambda\rangle\langle f\|C^{(\lambda)}\|f\rangle\left(\frac{4\pi}{2t+1}\right)^{\frac{1}{2}} \times\sum_j\frac{\left[\left(2\beta_j\right)^{t+1}\alpha_{OP,j}+\alpha_j'\right]}{R_j^{t+1}}\left(Y_p^{t*}\right)_j\delta_{t,\lambda+1} \tag{S3}$$

being $t$ and $p$ the ranks and components of the complex conjugate of the spherical harmonics $\left(Y_p^{t*}\right)$. The $\rho$ is the overlap integral between the valence subshells of the ligating atom and the 4*f* subshell of the lanthanide ion in the case of $Ln^{3+}$–O chemical bonds, they were obtained using the parametric approach in Ref. [14]. $\beta = 1/(1\pm\rho)$ is a parameter that defines the centroid of the electronic density of the chemical bond Ln–X (X= ligating atom) and $g$ is known as charge factor, which the product $\rho eg$ represents the electronic charge shared of the Ln–X chemical bond. Eq. S2 is the expression of the Simple Overlap Model (SOM) for the odd-ranked ligand field. [15,16] In Eq. S3, the Bond Overlap Model (BOM) for the Dynamic Coupling mechanism is used. [12,17]

The $\Omega_\lambda$ values, as well as the quantities obtained using the *JOYSpectra* program [18] ($g$, $\rho$, and $R$), are presented in Table S 5 where each ligating atom label is the same as

illustrated in Figure S10b. The sets of $\Omega_\lambda$ (in units of $10^{-20}$ cm$^2$) obtained are {$\Omega_2$ = 4.93; $\Omega_4$ = 3.33; $\Omega_6$ = 0.24} and {$\Omega_2$ = 16.97; $\Omega_4$ = 6.88; $\Omega_6$ = 0.36} for complexes **1** and **2**, respectively. The FED contributions are (in units of $10^{-20}$ cm$^2$) {$\Omega_2^{FED}$ = 0.004; $\Omega_4^{FED}$ = 0.048; $\Omega_6^{FED}$ = 0.075} and {$\Omega_2^{FED}$ = 0.012; $\Omega_4^{FED}$ = 0.042; $\Omega_6^{FED}$ = 0.059} for complexes **1** and **2**, respectively.

**Table S 5**. Values of $\rho$ (dimensionless), Ln–N bond distance $R$ (in Å), charge factor $g$ (dimensionless) and polarizabilities $\alpha'$ (in Å$^3$) used for the calculation of $\Omega_\lambda$ and the FED contribution (in $10^{-20}$ cm$^2$) for complexes **1** and **2**. The atoms label follows the same presented in Figure S10b.

| Ligating atom | $\rho$ (Eu–N) | $\rho$ (Tb–N) | $R$ | $g$ | $\alpha'$ |
|---|---|---|---|---|---|
| **N$_2$** | 0.038 | 0.058 | 2.62 | 0.76 | 1.14 |
| **N$_3$** | 0.051 | 0.067 | 2.47 | 0.42 | 0.30 |
| **N$_4$** | 0.050 | 0.067 | 2.48 | 0.42 | 0.30 |
| **N$_5$** | 0.041 | 0.060 | 2.58 | 0.76 | 1.14 |
| **N$_6$** | 0.051 | 0.068 | 2.46 | 0.42 | 0.30 |
| **N$_7$** | 0.038 | 0.058 | 2.62 | 0.76 | 1.14 |
| **N$_8$** | 0.051 | 0.067 | 2.47 | 0.42 | 0.30 |
| **N$_9$** | 0.050 | 0.067 | 2.48 | 0.42 | 0.30 |
| **N$_{10}$** | 0.051 | 0.068 | 2.46 | 0.42 | 0.30 |

### S2.3 Radiative rates and intensities

Once the theoretical intensity parameters $\Omega_\lambda$ were determined, it is possible to calculate the individual radiative rate $A_{J\to J'}$ (also known as spontaneous emission coefficients):

$$A_{J\to J'} = \frac{4e^2\left(\omega_{J\to J'}\right)^3}{3\hbar c^3(2J+1)}\left[\frac{n(n^2+2)^2}{9}S_{ed} + n^3 S_{md}\right] \quad \text{(S4)}$$

where,

$$S_{ed} = \sum_{\lambda=2,4,6} \Omega_\lambda \langle l^N \psi J \| U^{(\lambda)} \| l^N \psi' J' \rangle^2 \quad \text{(S5)}$$

$$S_{md} = \frac{\hbar}{4m_e^2 c^2}\langle l^N \psi J \| L + 2S \| l^N \psi' J' \rangle^2 \quad \text{(S6)}$$

are the electric and magnetic dipole strength, respectively. The squared matrix elements $\langle l^N \psi J \| U^{(\lambda)} \| l^N \psi' J' \rangle^2$ can be found in Ref. [19] and the $\langle l^N \psi J \| L + 2S \| l^N \psi' J' \rangle$ ($\Delta J$ = 0, ±1 with $J = J'$ = 0 excluded) for $Eu^{3+}$ and $Tb^{3+}$ can be calculated from the data in Ref. [20]. The $\omega_{J\to J'}$ is the angular frequency of the transition $|l^N \psi J\rangle \to |l^N \psi' J'\rangle$ ($^5D_0 \to {}^7F_J$, or

$^5D_4 \rightarrow {}^7F_{J'}$), $m_e$ is the electron mass, $n$ is the refractive index of the medium (considered here equal to 1.6). Summing up all radiative rates we obtain the total radiative rate $A_{rad} = 400$ and 680 $s^{-1}$ for complexes **1** and **2**, respectively.

The emissions of interest $^5D_0 \rightarrow {}^7F_2$ and $^5D_4 \rightarrow {}^7F_5$ can be calculated by:

$$I_{J \rightarrow J'} = A_{J \rightarrow J'} P_4 \tag{S7}$$

using the values of the emitting levels populations $P_4$ (in the steady-state regime) we can estimate the intensities $I_{Eu}$ and $I_{Tb}$ and, subsequently, the theoretical thermometric parameter $\Delta = \frac{I_{Tb}}{I_{Eu}}$. Thus,

$$\Delta = \frac{I_{Tb}}{I_{Eu}} = \frac{A_{4 \rightarrow 5} P_4(Tb)}{A_{0 \rightarrow 4} P_4(Eu)} \tag{S8}$$

where $A_{4 \rightarrow 5} = 478$ $s^{-1}$ and $A_{0 \rightarrow 4} = 59$ $s^{-1}$ obtained from Eq. S4.

### S2.4 Ligand-to-$Ln^{3+}$ energy transfer

The Jablonski-type energy level diagrams in Figure S 12 are useful to see the relative positions between donors (ligand's first singlet and triplet states, $S_1$ and $T_1$) and the 4f levels of the $Ln^{3+}$ ion ($Eu^{3+}$, $Tb^{3+}$, and $Dy^{3+}$). Level (or group of levels) are represented by ket $|n\rangle$ which each respective population ($\eta_n$) in the steady-state regime were solved using a rate equation model, as will be detailed in the next subsection. The dashed arrows illustrate where the energy comes from. For example, the dashed arrow indicated by $W_S$ in Figure S 12a implies that the $S_1$ is transferring energy to all upper levels of the $Eu^{3+}$ (from $^5D_0$ to $^5G_5$) as shown in pathways 1–15 in Table S 6.

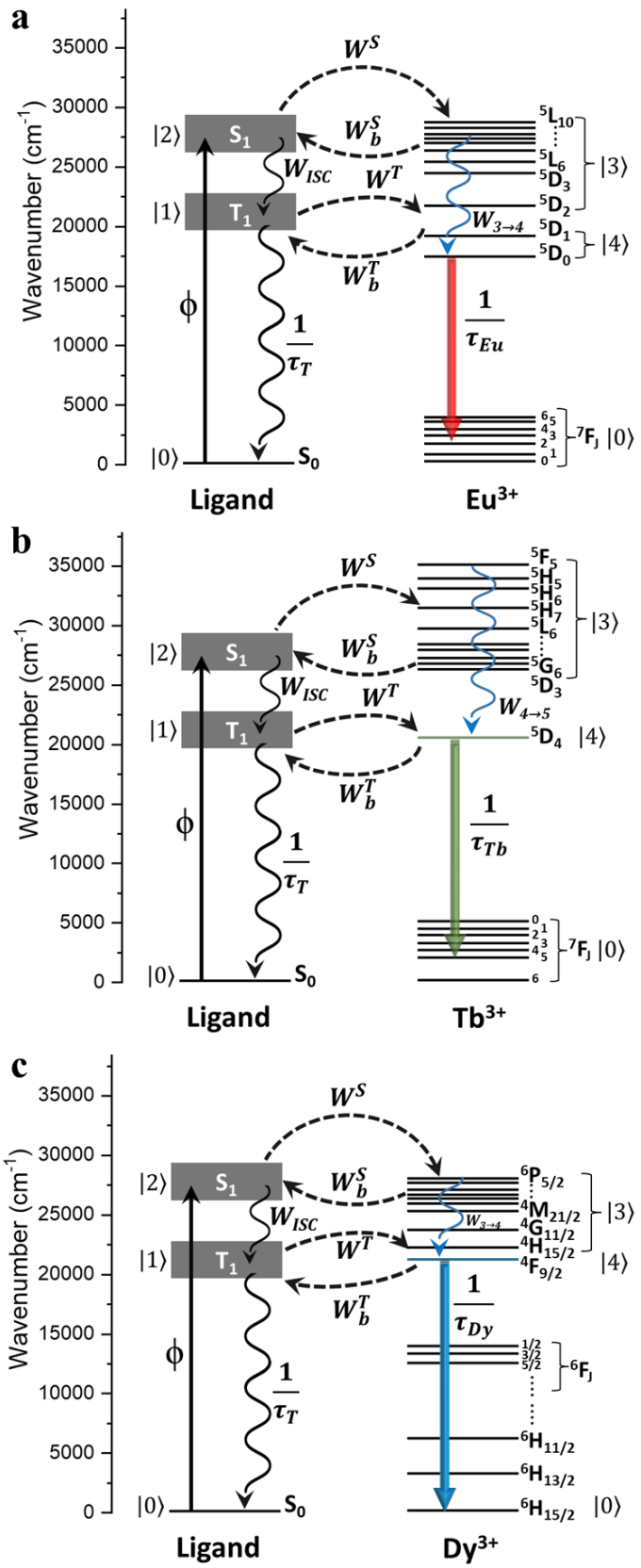


**Figure S 12**. Energy level diagrams for a) $Eu^{3+}$, b) $Tb^{3+}$, and c) $Dy^{3+}$ complexes. $\tau_T$, $\tau_S$, and $\tau_{Ln}$ are the decay lifetimes of the $T_1$, $S_1$, and $Ln^{3+}$ emitting levels ($^5D_0$, $^5D_4$, and $^4F_{9/2}$). $W_{3\to4}$ is the decay rate from $Ln^{3+}$ upper levels $|3\rangle$ to the emitting levels $|4\rangle$. $W_{ISC}$ is the $S_1 \to T_1$ intersystem crossing rate. $W^T$ and $W^S$ are the ligand-to-$Ln^{3+}$ energy transfer rates and $W_b^T$ and $W_b^S$ are their respective backward rates ($Ln^{3+}$-to-ligand). $\phi$ is the pumping rate from the ground state of the ligand $S_0$ to the excited $S_1$.

The intramolecular energy transfer rates (IET) from the excited states $S_1$ and $T_1$ to the $Ln^{3+}$ ion can be calculated taking into account the dipole-dipole ($W_{d-d}$), dipole-multipole ($W_{d-m}$), and exchange ($W_{ex}$) mechanisms [13,21,22],

$$W_{d-d} = \frac{S_L(1-\sigma_1)^2}{(2J+1)G}\frac{4\pi}{\hbar}\frac{e^2}{R_L^6}\sum_{\lambda}\Omega_K^{FED}\langle\psi' J'\|U^{(K)}\|\psi J\rangle^2 F \tag{S9}$$

$$W_{d-m} = \frac{S_L}{(2J+1)G}\frac{2\pi e^2}{\hbar}\sum_{K}(K+1)\frac{\langle r^K\rangle^2}{(R_L^{K+2})^2}\langle f\|C^{(K)}\|f\rangle^2(1-\sigma_K)^2 \times \langle\psi' J'\|U^{(K)}\|\psi J\rangle^2 F \tag{S10}$$

$$W_{ex} = \frac{(1-\sigma_0)^2}{(2J+1)G}\frac{8\pi}{\hbar}\frac{e^2}{R_L^4}\langle\psi' J'\|S\|\psi J\rangle^2\sum_{m}\left|\langle\phi|\sum_j \mu_z(j)s_m(j)\,|\phi^*\rangle\right|^2 F \tag{S11}$$

where $R_L$ is the donor–acceptor states distance. The $\Omega_K^{FED}$ (in Eq. S9) are the intensity parameters with the contribution of the forced electric dipole mechanism (considering only the Eq. S2 into Eq S1) as treated originally in the Judd-Ofelt theory [8,9]. The quantities $\langle\psi' J'\|U^{(K)}\|\psi J\rangle$ are reduced matrix elements and their values are tabulated in Ref. [19]. The $S_L$ is the dipole strength of the donor state involved in IET (with typical values in the order of $10^{-36}$–$10^{-38}$ and $10^{-40}$–$10^{-42}$ $(esu)^2{\cdot}cm^2$ for $S_1$ and $T_1$, respectively [13,23]). The $\langle r^K\rangle$ are the $4f$ radial integrals [24,25], $G$ is the state degeneracy (equal 1 for $S_1$ and 3 for $T_1$), and $(1-\sigma_K)$ are the shielding factors [14,26,27].

In Eq. S11, $s_m$ is the spin operator in the ligand, $\mu_z$ is the dipole operator (its $z$-component), the sum over $m$ leads values in the order of $10^{-36}$–$10^{-38}$ $(esu)^2{\cdot}cm^2$. The $\langle\psi' J'\|S\|\psi J\rangle$ is the reduced matrix elements of the spin operator from the $Ln^{3+}$ side, which were calculated using free-ion wavefunctions in the intermediate coupling scheme [20,22].

The $F$ term, in Eqs. S9–S11, is the spectral overlap factor that contains the energy mismatch conditions. Once the bandwidth at half-height for the ligands ($\gamma_L$) is much larger than the lanthanides ($\gamma_{Ln}$), $\gamma_L \gg \gamma_{Ln}$, this factor can simply obtained as follows [13]:

$$F = \frac{1}{\hbar\gamma_L}\sqrt{\frac{\ln(2)}{\pi}}\,e^{-\left(\frac{\delta}{\hbar\gamma_L}\right)^2\ln(2)} \tag{S12}$$

where δ is the band maximum energy difference between donor state ($E_D$) and lanthanide ion acceptor state ($E_{Ln}$), $\delta = E_D - E_{Ln}$.

The forward energy transfer rates ($W$) involving the $Ln^{3+}$ as acceptor are calculated by the sum over all mechanisms in the same pathway:

$$W = W_{d-d} + W_{d-m} + W_{ex} \quad \text{(S13)}$$

The backward energy transfer rates ($W_b$), that is, the energy returned from acceptor to donor state, are obtained with the same above equations, except for multiplying the energy mismatch conditions factors $F$ (Eq. S12) by the Boltzmann's energy barrier factor,

$$F_b = F e^{-\left(\frac{|\delta|}{k_B T}\right)} \quad \text{(S14)}$$

where $T$ is the temperature and $k_B$ is the Boltzmann's constant.

The IET rates for complexes **1**, **2**, and **3** at 300 K are displayed in Table S 6, Table S 7, and Table S 8, respectively. It can be noted that the forward energy transfer via $T_1 \rightarrow Eu^{3+}$ ($W^T$ in Table S 6) is higher than the $S_1 \rightarrow Eu^{3+}$ one ($W^S$ in Table S 6) indicating that the main energy transfer for the $Eu^{3+}$ complex is via ligand's $T_1$. Also, the backward rate $W_b^T$ is more than four times higher than the $W_b^S$ (Table S 6**)**. However, the complex **1** has a positive balance between forward and backward rates ($W^S > W_b^S$ and $W^T > W_b^T$), contrarily, complexes **2** and **3** presented $W_b^T > W^T$ which may be the main reason for the relative low emission quantum yield of the complex **2** ($Q_{Tb}^L$) and the presence of the ligand emission of the complex **3** (Figure S6C). The trend of $W_b^T > W^T$ for complexes **2** and **3** was also found in the calculations varying the temperature, as depicted in Figure S 13.

**Table S 6**. Energy transfer rates (in $s^{-1}$) from ligands to $Eu^{3+}$ (complex **1**). The δ is the donor–acceptor energy difference (in $cm^{-1}$). $W_{d-d}$, $W_{d-m}$, and $W_{ex}$ are the dipole-dipole, dipole-multipole, and exchange rates, respectively. $W$ and $W_b$ are the forward and backward energy transfer rates for each pathway at 300 K.

| pathway label | donor | acceptor | $\delta$ | $W_{d-d}$ | $W_{d-m}$ | $W_{ex}$ | $W$ (forward) | $W_b$ (backward) |
|---|---|---|---|---|---|---|---|---|
| 1 | $S_1$ | $^7F_0 \rightarrow {}^5D_0$ | 9587 | 3.19E-2 | 2.86E+3 | 0 | 4.79 | 5.15E-20 |
| 2 | $S_1$ | $^7F_0 \rightarrow {}^5D_1$ | 7853 | 0 | 0 | 3.42E+5 | 2.29E+5 | 1.01E-11 |
| 3 | $S_1$ | $^7F_0 \rightarrow {}^5L_6$ | 1555 | 1.07E+4 | 1.39E+3 | 0 | 8.11E+3 | 4.68 |
| 4 | $S_1$ | $^7F_0 \rightarrow {}^5G_6$ | 128 | 3.12E+3 | 4.05E+2 | 0 | 2.36E+3 | 1.28E+3 |
| 5 | $S_1$ | $^7F_0 \rightarrow {}^5D_4$ | -706 | 5.66E+2 | 9.88E+3 | 0 | 2.37E+2 | 7.00E+3 |
| 6 | $S_1$ | $^7F_1 \rightarrow {}^5D_0$ | 9959 | 0 | 0 | 2.69E+4 | 8.87E+3 | 1.60E-17 |
| 7 | $S_1$ | $^7F_1 \rightarrow {}^5D_1$ | 8225 | 6.90E-2 | 6.17E+3 | 7.38E+1 | 2.06E+3 | 1.52E-14 |
| 8 | $S_1$ | $^7F_1 \rightarrow {}^5D_2$ | 5769 | 0 | 0 | 4.05E+5 | 1.34E+5 | 1.29E-7 |
| 9 | $S_1$ | $^7F_1 \rightarrow {}^5D_3$ | 2897 | 1.13E+2 | 9.67E+4 | 0 | 3.20E+4 | 2.96E-2 |
| 10 | $S_1$ | $^7F_1 \rightarrow {}^5L_6$ | 1927 | 1.92E+3 | 2.50E+2 | 0 | 7.18E+2 | 6.96E-2 |
| 11 | $S_1$ | $^7F_1 \rightarrow {}^5L_7$ | 895 | 4.79E+3 | 6.21E+2 | 0 | 1.79E+3 | 2.44E+1 |
| 12 | $S_1$ | $^7F_1 \rightarrow {}^5G_2$ | 860 | 0 | 0 | 5.52E+6 | 1.82E+6 | 2.95E+4 |
| 13 | $S_1$ | $^7F_1 \rightarrow {}^5G_3$ | 630 | 2.09E+2 | 9.13E+4 | 0 | 3.02E+4 | 1.47E+3 |
| 14 | $S_1$ | $^7F_1 \rightarrow {}^5G_6$ | 500 | 1.35E+3 | 1.75E+2 | 0 | 5.05E+2 | 4.59E+1 |
| 15 | $S_1$ | $^7F_1 \rightarrow {}^5G_5$ | 489 | 2.75E+3 | 1.57E+3 | 0 | 1.43E+3 | 1.37E+2 |
| | | | | | | **$W^S$** | **2.27E+6** | |
| | | | | | | **$W_b^S$** | | **3.94E+4** |
| 16 | $T_1$ | $^7F_0 \rightarrow {}^5D_0$ | 4607 | 2.46E-2 | 2.20E+3 | 0 | 3.69 | 9.36E-10 |
| 17 | $T_1$ | $^7F_0 \rightarrow {}^5D_1$ | 2873 | 0 | 0 | 6.98E+6 | 4.67E+6 | 4.85 |
| 18 | $T_1$ | $^7F_0 \rightarrow {}^5L_6$ | -3425 | 1.74E+1 | 2.26 | 0 | 9.70E-7 | 1.32E+1 |
| 19 | $T_1$ | $^7F_0 \rightarrow {}^5G_6$ | -4852 | 1.70 | 2.20E-1 | 0 | 1.01E-10 | 1.29 |
| 20 | $T_1$ | $^7F_0 \rightarrow {}^5D_4$ | -5686 | 1.63E-1 | 2.84 | 0 | 2.88E-12 | 2.01 |
| 21 | $T_1$ | $^7F_1 \rightarrow {}^5D_0$ | 4979 | 0 | 0 | 2.76E+6 | 9.10E+5 | 3.88E-5 |
| 22 | $T_1$ | $^7F_1 \rightarrow {}^5D_1$ | 3245 | 1.87E-2 | 1.67E+3 | 2.00E+3 | 1.21E+3 | 2.12E-4 |
| 23 | $T_1$ | $^7F_1 \rightarrow {}^5D_2$ | 789 | 0 | 0 | 1.67E+6 | 5.52E+5 | 1.25E+4 |
| 24 | $T_1$ | $^7F_1 \rightarrow {}^5D_3$ | -2083 | 5.16E-1 | 4.41E+2 | 0 | 6.68E-3 | 1.46E+2 |
| 25 | $T_1$ | $^7F_1 \rightarrow {}^5L_6$ | -3053 | 4.16 | 5.40E-1 | 0 | 6.80E-7 | 1.55 |
| 26 | $T_1$ | $^7F_1 \rightarrow {}^5L_7$ | -4085 | 4.70 | 6.09E-1 | 0 | 5.43E-9 | 1.75 |
| 27 | $T_1$ | $^7F_1 \rightarrow {}^5G_2$ | -4120 | 0 | 0 | 5.27E+5 | 4.56E-4 | 1.74E+5 |
| 28 | $T_1$ | $^7F_1 \rightarrow {}^5G_3$ | -4350 | 1.67E-1 | 7.31E+1 | 0 | 2.11E-8 | 2.42E+1 |
| 29 | $T_1$ | $^7F_1 \rightarrow {}^5G_6$ | -4480 | 9.80E-1 | 1.27E-1 | 0 | 1.71E-10 | 3.66E-1 |
| 30 | $T_1$ | $^7F_1 \rightarrow {}^5G_5$ | -4491 | 1.98 | 1.13 | 0 | 4.53E-10 | 1.02 |
| | | | | | | **$W^T$** | **6.14E+6** | |
| | | | | | | **$W_b^T$** | | **1.87E+5** |

**Table S 7**. Energy transfer rates (in $s^{-1}$) from ligands to $Tb^{3+}$ (complex **2**). The δ is the donor–acceptor energy difference (in $cm^{-1}$). $W_{d-d}$, $W_{d-m}$, and $W_{ex}$ are the dipole-dipole, dipole-multipole, and exchange rates, respectively. $W$ and $W_b$ are the forward and backward energy transfer rates for each pathway at 300 K.

| pathway label | donor | acceptor | $\delta$ | $W_{d-d}$ | $W_{d-m}$ | $W_{ex}$ | $W$ (forward) | $W_b$ (backward) |
|---|---|---|---|---|---|---|---|---|
| 1 | $S_1$ | $^7F_6 \rightarrow {}^5D_4$ | 6436 | 6.55 | 6.05E+3 | 0 | 6.06E+3 | 2.38E-10 |
| 2 | $S_1$ | $^7F_6 \rightarrow {}^5D_3$ | 644 | 1.30E+2 | 9.94E+1 | 0 | 2.29E+2 | 1.04E+1 |
| 3 | $S_1$ | $^7F_6 \rightarrow {}^5G_6$ | 457 | 1.02E+4 | 2.59E+5 | 1.06E+8 | 1.06E+8 | 1.19E+7 |
| 4 | $S_1$ | $^7F_6 \rightarrow {}^5L_{10}$ | -91 | 5.09E+3 | 4.24E+2 | 0 | 3.57E+3 | 5.52E+3 |
| 5 | $S_1$ | $^7F_6 \rightarrow {}^5G_5$ | -887 | 1.18E+3 | 1.85E+5 | 6.97E+6 | 1.02E+5 | 7.16E+6 |
| 6 | $S_1$ | $^7F_6 \rightarrow {}^5G_4$ | -1407 | 6.69E+2 | 1.42E+4 | 0 | 1.74E+1 | 1.48E+4 |
| 7 | $S_1$ | $^7F_6 \rightarrow {}^5L_6$ | -2730 | 0 | 0 | 9.81E+5 | 2.02 | 9.81E+5 |
| 8 | $S_1$ | $^7F_6 \rightarrow {}^5H_7$ | -4499 | 0 | 0 | 4.08E+5 | 1.74E-4 | 4.08E+5 |
| 9 | $S_1$ | $^7F_6 \rightarrow {}^5H_6$ | -6011 | 0 | 0 | 9.69E+5 | 2.93E-7 | 9.69E+5 |
| 10 | $S_1$ | $^7F_6 \rightarrow {}^5H_5$ | -6887 | 0 | 0 | 4.48E-3 | 2.02E-17 | 4.48E-3 |
| 11 | $S_1$ | $^7F_6 \rightarrow {}^5F_5$ | -8054 | 0 | 0 | 2.17E+5 | 3.64E-12 | 2.17E+5 |
| 12 | $S_1$ | $^7F_5 \rightarrow {}^5D_4$ | 8484 | 1.27 | 1.07E+4 | 4.60E+4 | 5.67E+4 | 1.21E-13 |
| 13 | $S_1$ | $^7F_5 \rightarrow {}^5D_3$ | 2692 | 2.01E+2 | 5.60E+4 | 0 | 5.62E+4 | 1.39E-1 |
| 14 | $S_1$ | $^7F_5 \rightarrow {}^5G_6$ | 2505 | 7.10E+2 | 4.76E+5 | 1.03E+7 | 1.08E+7 | 6.55E+1 |
| 15 | $S_1$ | $^7F_5 \rightarrow {}^5L_{10}$ | 1957 | 1.16E+2 | 6.39 | 0 | 1.22E+2 | 1.02E-2 |
| 16 | $S_1$ | $^7F_5 \rightarrow {}^5G_5$ | 1161 | 6.18E+2 | 1.75E+4 | 5.03E+7 | 5.04E+7 | 1.92E+5 |
| 17 | $S_1$ | $^7F_5 \rightarrow {}^5G_4$ | 641 | 2.11E+2 | 9.33E+4 | 6.86E+6 | 6.95E+6 | 3.21E+5 |
| 18 | $S_1$ | $^7F_5 \rightarrow {}^5L_6$ | -682 | 0 | 0 | 2.71E+5 | 1.03E+4 | 2.71E+5 |
| 19 | $S_1$ | $^7F_5 \rightarrow {}^5H_6$ | -3963 | 0 | 0 | 7.13E+5 | 3.97E-3 | 7.13E+5 |
| 20 | $S_1$ | $^7F_5 \rightarrow {}^5H_5$ | -4839 | 0 | 0 | 4.92E+6 | 4.11E-4 | 4.92E+6 |
| 21 | $S_1$ | $^7F_5 \rightarrow {}^5F_5$ | -6006 | 0 | 0 | 2.46E+6 | 7.60E-7 | 2.46E+6 |
| | | | | | | $W^S$ | **1.75E+8** | |
| | | | | | | $W_b^S$ | | **3.05E+7** |
| 22 | $T_1$ | $^7F_6 \rightarrow {}^5D_4$ | 1456 | 4.51E-1 | 4.16E+2 | 0 | 4.17E+2 | 3.87E-1 |
| 23 | $T_1$ | $^7F_6 \rightarrow {}^5D_3$ | -4336 | 1.05E-1 | 8.04E-2 | 0 | 1.72E-10 | 1.85E-1 |
| 24 | $T_1$ | $^7F_6 \rightarrow {}^5G_6$ | -4523 | 7.18 | 1.82E+2 | 7.44E+6 | 2.83E-3 | 7.44E+6 |
| 25 | $T_1$ | $^7F_6 \rightarrow {}^5L_{10}$ | -5071 | 2.34 | 1.95E-1 | 0 | 6.96E-11 | 2.54 |
| 26 | $T_1$ | $^7F_6 \rightarrow {}^5G_5$ | -5867 | 2.94E-1 | 4.62E+1 | 1.74E+5 | 1.05E-7 | 1.74E+5 |
| 27 | $T_1$ | $^7F_6 \rightarrow {}^5G_4$ | -6387 | 1.12E-1 | 2.37 | 0 | 1.24E-13 | 2.49 |
| 28 | $T_1$ | $^7F_6 \rightarrow {}^5L_6$ | -7710 | 0 | 0 | 5.96E+3 | 5.21E-13 | 5.96E+3 |
| 29 | $T_1$ | $^7F_6 \rightarrow {}^5H_7$ | -9479 | 0 | 0 | 6.39E+2 | 1.15E-17 | 6.39E+2 |
| 30 | $T_1$ | $^7F_6 \rightarrow {}^5H_6$ | -10991 | 0 | 0 | 4.75E+2 | 6.09E-21 | 4.75E+2 |
| 31 | $T_1$ | $^7F_6 \rightarrow {}^5H_5$ | -11867 | 0 | 0 | 1.12E-6 | 2.15E-31 | 1.12E-6 |
| 32 | $T_1$ | $^7F_6 \rightarrow {}^5F_5$ | -13034 | 0 | 0 | 2.22E+1 | 1.58E-26 | 2.22E+1 |
| 33 | $T_1$ | $^7F_5 \rightarrow {}^5D_4$ | 3504 | 4.21E-1 | 3.54E+3 | 1.52E+6 | 1.52E+6 | 7.67E-2 |
| 34 | $T_1$ | $^7F_5 \rightarrow {}^5D_3$ | -2288 | 7.82E-1 | 2.18E+2 | 0 | 3.75E-3 | 2.19E+2 |
| 35 | $T_1$ | $^7F_5 \rightarrow {}^5G_6$ | -2475 | 2.39 | 1.61E+3 | 3.48E+6 | 2.44E+1 | 3.49E+6 |
| 36 | $T_1$ | $^7F_5 \rightarrow {}^5L_{10}$ | -3023 | 2.56E-1 | 1.41E-2 | 0 | 1.36E-7 | 2.70E-1 |
| 37 | $T_1$ | $^7F_5 \rightarrow {}^5G_5$ | -3819 | 7.44E-1 | 2.10E+1 | 6.06E+6 | 6.73E-2 | 6.06E+6 |
| 38 | $T_1$ | $^7F_5 \rightarrow {}^5G_4$ | -4339 | 1.70E-1 | 7.53E+1 | 5.54E+5 | 5.08E-4 | 5.54E+5 |
| 39 | $T_1$ | $^7F_5 \rightarrow {}^5L_6$ | -5662 | 0 | 0 | 7.91E+3 | 1.27E-8 | 7.91E+3 |
| 40 | $T_1$ | $^7F_5 \rightarrow {}^5H_6$ | -8943 | 0 | 0 | 1.68E+3 | 3.98E-16 | 1.68E+3 |
| 41 | $T_1$ | $^7F_5 \rightarrow {}^5H_5$ | -9819 | 0 | 0 | 5.94E+3 | 2.10E-17 | 5.94E+3 |
| 42 | $T_1$ | $^7F_5 \rightarrow {}^5F_5$ | -10986 | 0 | 0 | 1.21E+3 | 1.59E-20 | 1.21E+3 |
| | | | | | | $W^T$ | **1.52E+6** | |
| | | | | | | $W_b^T$ | | **1.77E+7** |

**Table S 8**. Energy transfer rates (in $s^{-1}$) from ligands to $Dy^{3+}$ (complex **3**). The δ is the donor–acceptor energy difference (in $cm^{-1}$). $W_{d-d}$, $W_{d-m}$, and $W_{ex}$ are the dipole-dipole, dipole-multipole, and exchange rates, respectively. $W$ and $W_b$ are the forward and backward energy transfer rates for each pathway at 300 K.

| pathway label | donor | acceptor | $\delta$ | $W_{d-d}$ | $W_{d-m}$ | $W_{ex}$ | $W$ (forward) | $W_b$ (backward) |
|---|---|---|---|---|---|---|---|---|
| 1 | $S_1$ | $^6H_{15/2}\rightarrow{}^4F_{9/2}$ | 5827 | 2.02E+2 | 1.39E+2 | 0 | 3.42E+2 | 2.50E-10 |
| 2 | $S_1$ | $^6H_{15/2}\rightarrow{}^4H_{15/2}$ | 4833 | 9.42E+2 | 1.91E+5 | 1.27E+6 | 1.46E+6 | 1.26E-4 |
| 3 | $S_1$ | $^6H_{15/2}\rightarrow{}^4G_{11/2}$ | 3492 | 3.14E+2 | 2.75E+4 | 0 | 2.78E+4 | 1.48E-3 |
| 4 | $S_1$ | $^6H_{15/2}\rightarrow{}^4M_{21/2}$ | 1946 | 5.61E+3 | 3.18E+3 | 0 | 8.79E+3 | 7.77E-1 |
| 5 | $S_1$ | $^6H_{15/2}\rightarrow{}^4I_{13/2}$ | 1261 | 1.96E+3 | 5.60E+5 | 1.22E+7 | 1.28E+7 | 3.02E+4 |
| 6 | $S_1$ | $^6H_{15/2}\rightarrow{}^4F_{7/2}$ | 1199 | 5.43E+3 | 2.43E+4 | 0 | 2.97E+4 | 9.47E+1 |
| 7 | $S_1$ | $^6H_{15/2}\rightarrow{}^4K_{17/2}$ | 1165 | 7.23E+3 | 1.48E+6 | 0 | 1.48E+6 | 5.56E+3 |
| 8 | $S_1$ | $^6H_{15/2}\rightarrow{}^4M_{19/2}$ | 721 | 8.74E+3 | 3.67E+4 | 0 | 4.55E+4 | 1.43E+3 |
| 9 | $S_1$ | $^6H_{15/2}\rightarrow{}^6P_{3/2}$ | -488 | 4.29E+3 | 1.96E+2 | 0 | 4.32E+2 | 4.49E+3 |
| 10 | $S_1$ | $^6H_{15/2}\rightarrow{}^6P_{5/2}$ | -569 | 6.05E+3 | 2.77E+2 | 0 | 4.13E+2 | 6.33E+3 |
| | | | | | | $W^S$ | **1.58E+7** | |
| | | | | | | $W_b^S$ | | **4.81E+4** |
| 11 | $T_1$ | $^6H_{15/2}\rightarrow{}^4F_{9/2}$ | 847 | 8.72 | 6.01 | 0 | 1.47E+1 | 2.54E-1 |
| 12 | $T_1$ | $^6H_{15/2}\rightarrow{}^4H_{15/2}$ | -147 | 1.89E+1 | 3.83E+3 | 2.56E+6 | 1.27E+6 | 2.56E+6 |
| 13 | $T_1$ | $^6H_{15/2}\rightarrow{}^4G_{11/2}$ | -1488 | 2.25 | 1.98E+2 | 0 | 1.59E-1 | 2.00E+2 |
| 14 | $T_1$ | $^6H_{15/2}\rightarrow{}^4M_{21/2}$ | -3034 | 1.23E+1 | 6.97 | 0 | 9.25E-6 | 1.93E+1 |
| 15 | $T_1$ | $^6H_{15/2}\rightarrow{}^4I_{13/2}$ | -3719 | 2.54 | 7.27E+2 | 1.59E+6 | 2.85E-2 | 1.59E+6 |
| 16 | $T_1$ | $^6H_{15/2}\rightarrow{}^4F_{7/2}$ | -3781 | 6.72 | 3.01E+1 | 0 | 4.91E-7 | 3.68E+1 |
| 17 | $T_1$ | $^6H_{15/2}\rightarrow{}^4K_{17/2}$ | -3815 | 8.72 | 1.78E+3 | 0 | 2.03E-5 | 1.79E+3 |
| 18 | $T_1$ | $^6H_{15/2}\rightarrow{}^4M_{19/2}$ | -4259 | 7.50 | 3.15E+1 | 0 | 5.25E-8 | 3.90E+1 |
| 19 | $T_1$ | $^6H_{15/2}\rightarrow{}^6P_{3/2}$ | -5468 | 1.46 | 6.66E-2 | 0 | 6.22E-12 | 1.52 |
| 20 | $T_1$ | $^6H_{15/2}\rightarrow{}^6P_{5/2}$ | -5549 | 1.93 | 8.82E-2 | 0 | 5.59E-12 | 2.02 |
| | | | | | | $W^T$ | **1.27E+6** | |
| | | | | | | $W_b^T$ | | **4.15E+6** |

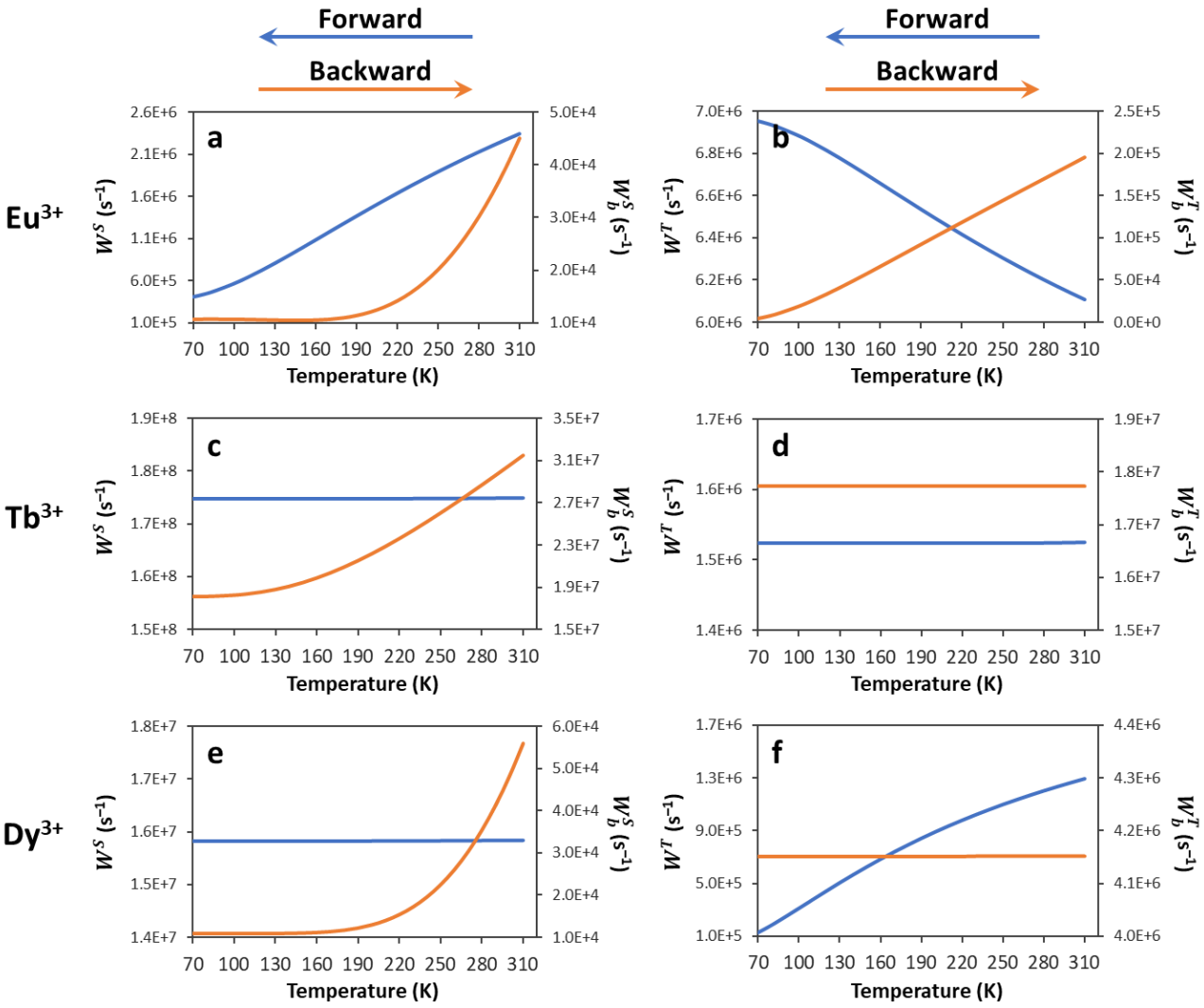


**Figure S 13**. Energy transfer rates (in $s^{-1}$) as a function of the temperature (in K). The left-side and the right-side scales represent the forward ($W^S$ and $W^T$) and backward ($W_b^S$ and $W_b^T$) IET rates, respectively. (a-b) involves the complex **1** ($Eu^{3+}$), (c-d) complex **2** ($Tb^{3+}$), and (e-f) complex **3** ($Dy^{3+}$).

### S2.5 Rate equations

Once the IET rates with the temperature are determined (see Figure S 13), we can construct a rate equations model to estimate the emitting level population in the steady-state regime as follows:

$$\frac{d}{dt}P_0(t) = \frac{1}{\tau_T}P_1(t) + \frac{1}{\tau_S}P_2(t) + \frac{1}{\tau_{Ln}}P_4(t) - \phi P_0(t) \quad \text{(S15)}$$

$$\frac{d}{dt}P_1(t) = W_{ISC}P_2(t) + W_b^T P_3(t) - \left(\frac{1}{\tau_T} + W^T\right)P_1(t) \quad \text{(S16)}$$

$$\frac{d}{dt}P_2(t) = \phi P_0(t) + W_b^S P_3(t) - \left(\frac{1}{\tau_S} + W_{ISC} + W^S\right)P_2(t) \quad \text{(S17)}$$

$$\frac{d}{dt}P_3(t) = W^S P_2(t) - (W_{3\to4} + W_b^T + W_b^S)P_3(t) \quad \text{(S18)}$$

$$\frac{d}{dt}P_4(t) = W_{3\to4}P_3(t) + W^T P_1(t) - \frac{1}{\tau_{Ln}}P_4(t) \quad \text{(S19)}$$

where $\tau_T$, $\tau_S$, and $\tau_{Ln}$ are the decay lifetimes of the $T_1$, $S_1$, and $Ln^{3+}$ emitting levels, respectively. $W_{3\to4} \approx 10^6$ $s^{-1}$ is the decay rate from $Ln^{3+}$ upper levels (represented by the group of states $|3\rangle$ in Figure S 12) to the emitting levels ($|4\rangle$ in Figure S 12). $W_{ISC}$ is the $S_1 \to T_1$ intersystem crossing rate. $W^T$ and $W^S$ are the ligand-to-$Ln^{3+}$ energy transfer rates and $W_b^T$ and $W_b^S$ are their respective backward rates ($Ln^{3+}$-to-ligand). It is worth to mention that a normalized population ($\sum P_n(t) = 1$) is considered in the equations above and only the ground state is populated before the excitation ($P_0(t) = 1$ for $t = 0$).

The pumping rate $\phi = 188$ $s^{-1}$ was estimated using the relation,

$$\phi = \frac{\sigma\rho\lambda_{exc}}{hc} \quad \text{(S20)}$$

where $\sigma$ (~$10^{-16}$ $cm^2$) is the absorption cross-section of the organic chromophores, $\rho$ (~ 1 $W/cm^{-2}$) is the power density of the excitation source at $\lambda_{exc}$ = 372 nm. If the power density is increased to $\rho = 10$ $W/cm^{-2}$, $\phi = 1880\ s^{-1}$ and this causes a higher depopulation of the ground-level ($P_0$, Eq. S15) and increases other populations, mainly the $T_1$ and $Ln^{3+}$ emitting levels. However, at the steady-state regime, the ratio $P_n/\phi P_0$

($n \neq 0$) is still the same as $\rho = 1$ W/cm$^{-2}$. This is the reason why the emission quantum yield is independent of the power density, at least for ranges of low power density that do not affect the photostability of the compound.

The set of rate equations (Eqs S15–S19) were numerically solved using the Radau method.[28] Each simulation consists of a time propagation from 0 to 0.1 s with a step size of $2\times10^{-6}$ (total of $5\times10^{4}$ points).

**S2.6 Emission quantum yields**

The emission quantum yield ($Q_{Ln}^{L}$) is the rate between emitted and absorbed photons. In the Ln-based complexes, the absorption is given predominantly by the ligands due to their high absorption cross-section while the emission is from $Ln^{3+}$ ions. Thus, the $Q_{Ln}^{L}$ can be calculated as:

$$Q_{Ln}^{L} = \frac{Number\ of\ emitted\ photons}{Number\ of\ absorbed\ photons} = \frac{A_{rad}P_4}{\phi P_0} \quad \text{(S21)}$$

where $A_{rad}$ (400 and 680 s$^{-1}$ for complexes **1** and **2**) is the radiative rate (see **SS2.3 Radiative rates and intensities**) from the $Ln^{3+}$ emitting level with population fraction $P_4$. $P_0$ is the ground state population fraction and $\phi$ is the pumping rate (Eq. S20).

When variations on $\tau_T$, $\tau_S$, and $W_{ISC}$ within acceptable physical values are done, we noted that the $Q_{Ln}^{L}$ is only sensitive to the $\tau_T$ lifetime close to the microseconds limit (Figure S 14). This is a direct consequence of the IET rates involving the T1 state ($W^T$ and $W_b^T$) being in the order $10^6$ s$^{-1}$, becoming the $\tau_T$ competitive with them only when approaching the faster limit. On the other hand, the $Q_{Ln}^{L}$ showed to be very sensitive to the changes in $\tau_S$ (Figure 4). The $W_{ISC}$ almost does not affect the complex **2** and this is related to the $S_1 \rightarrow Tb^{3+}$ IET rate ($W^S = 1.75 \times 10^8$ s$^{-1}$ at room temperature), which dominates the process due to relation $W^S > W_{ISC}$. It is worth to mention that the $W_{ISC}$ for energy difference $\Delta E_{S-T}$ around 5000 cm$^{-1}$ in Ln-based complexes could be in the order of $10^6$ and $10^7$ s$^{-1}$.

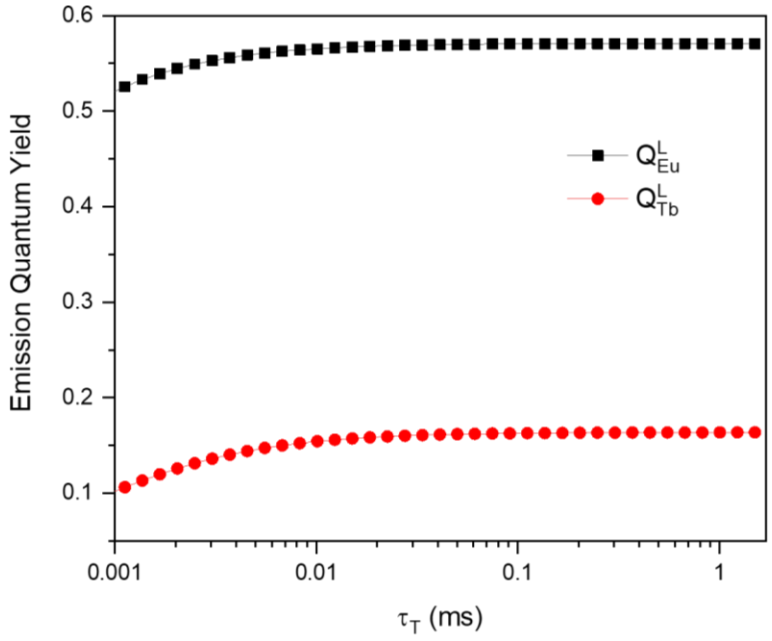


**Figure S 14**. Emission quantum yield for complexes **1** ($Q_{Eu}^{L}$) and **2** ($Q_{Tb}^{L}$)as a function of the $T_1$ lifetime. The values of $Q_{Ln}^{L}$ start to decrease when the $\tau_T$ becomes very short (~ $10^{-5}$ s). The values of $\tau_S = 6.7 \times 10^{-7}$ s and $W_{ISC} = 2.7 \times 10^{6}$ $s^{-1}$ were fixed based on their simultaneous variations as shows Figure 4.

## S3. Thermometric characterization

Relative thermal sensitivity ($S_r$):

$$S_r = \frac{1}{\Delta}\frac{\partial \Delta}{\partial T} \tag{S20}$$

Minimal temperature uncertainty ($\delta T$):

$$\delta T = \frac{1}{S_r}\frac{\delta \Delta}{\Delta} \tag{S21}$$

where $\delta\Delta$ is the uncertainty of the $\Delta$.

The $\delta\Delta$ was obtained considering the experimental uncertainty associated with the thermometric parameter as:

$$(\delta\Delta)^2 = \left(\frac{\partial \Delta}{\partial I_{Tb}}\delta I_{Tb}\right)^2 + \left(\frac{\partial \Delta}{\partial I_{Eu}}\delta I_{Eu}\right)^2 \tag{S22}$$

where $\delta I_{Tb}$ and $\delta I_{Eu}$ are the uncertainties associated to of $I_{Tb}$ and $I_{Eu}$, respectively. $\delta I_{Tb}$ and $\delta I_{Eu}$ were determined considering the noise level of the emission spectra.

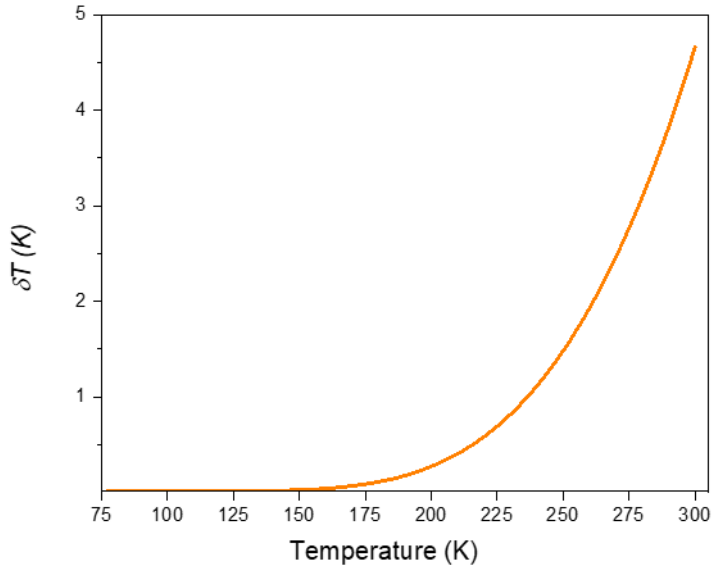


**Figure S 15**. Temperature uncertainty for the mixed **$Eu_{0.09}Tb_{0.91}$** complexes.

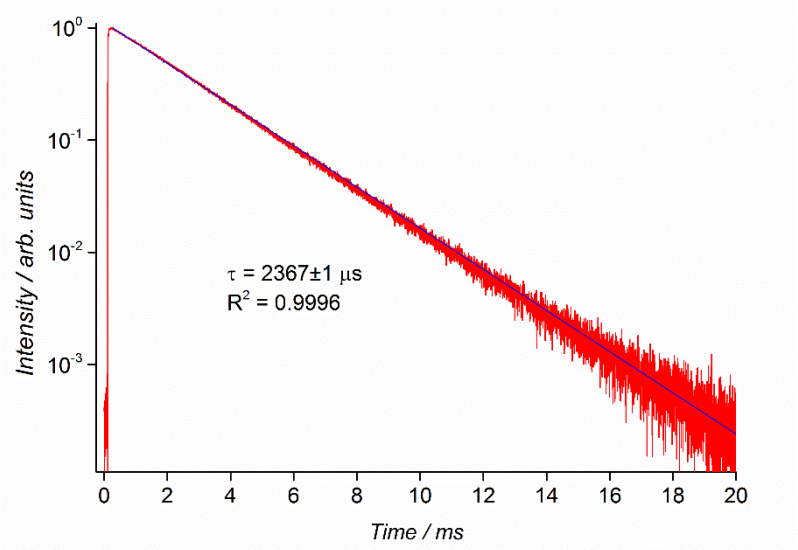


**Figure S 16**. Luminescence decay curve for the **$Eu_{0.09}Tb_{0.91}$** complexes monitored in the $Eu^{3+}$ $^5D_0 \rightarrow {}^7F_2$ transition at 360 nm. The decay reveals a single-exponential behavior suggesting that the energy transfer between $Tb^{3+}$ and $Eu^{3+}$ can be neglected. In addition, no rise in the decay curve was observed when the excitation source is turned off, confirming that the Tb-to-Eu energy transfer is not operative.

## References


[1] F. Neese, The ORCA program system, *WIREs Computational Molecular Science*, 2012, **2**, 73-78.

[2] L. Ungur and L. F. Chibotaru, *SINGLE_ANISO Program*, 2006-2013.

[3] M. J. Frisch, G. W. Trucks, H. B. Schlegel, G. E. Scuseria, M. A. Robb, J. R. Cheeseman, G. Scalmani, V. Barone, B. Mennucci, G. A. Petersson, H. Nakatsuji, M. Caricato, X. Li, H. P. Hratchian, A. F. Izmaylov, J. Bloino, G. Zheng, J. L. Sonnenberg, M. Hada, M. Ehara, K. Toyota, R. Fukuda, J. Hasegawa, M. Ishida, T. Nakajima, Y. Honda, O. Kitao, H. Nakai, T. Vreven, J. J. A. Montgomery, J. E. Peralta, F. Ogliaro, M. Bearpark, J. J. Heyd, E. Brothers, K. N. Kudin, V. N. Staroverov, T. Keith, R. Kobayashi, J. Normand, K. Raghavachari, A. Rendell, J. C. Burant, S. S. Iyengar, J. Tomasi, M. Cossi, N. Rega, J. M. Millam, M. Klene, J. E. Knox, J. B. Cross, V. Bakken, C. Adamo, J. Jaramillo, R. Gomperts, R. E. Stratmann, O. Yazyev, A. J. Austin, R. Cammi, C. Pomelli, J. W. Ochterski, R. L. Martin, K. Morokuma, V. G. Zakrzewski, G. A. Voth, P. Salvador, J. J. Dannenberg, S. Dapprich, A. D. Daniels, O. Farkas, J. B. Foresman, J. V. Ortiz, J. Cioslowski, D. J. Fox, **2013**.

[4] A. D. Becke, *J. Chem. Phys.* **1993**, *98*, 5648.

[5] C. Lee, W. Yang, R. G. Parr, *Phys. Rev. B* **1988**, *37*, 785.

[6] M. Dolg, H. Stoll, H. Preuss, *J. Chem. Phys.* **1989**, *90*, 1730.

[7] L. E. do N. Aquino, G. A. Barbosa, J. de L. Ramos, S. O. K. Giese, F. S. Santana, D. L. Hughes, G. G. Nunes, L. Fu, M. Fang, G. Poneti, A. N. Carneiro Neto, R. T. Moura, R. A. S. Ferreira, L. D. Carlos, A. G. Macedo, J. F. Soares, *Inorg. Chem.* **2021**, *60*, 892.

[8] B. R. Judd, *Phys. Rev.* **1962**, *127*, 750.

[9] G. S. Ofelt, *J. Chem. Phys.* **1962**, *37*, 511.

[10] C. K. Jørgensen, B. R. Judd, *Mol. Phys.* **1964**, *8*, 281.

[11] B. G. Wybourne, *Spectroscopic Properties of Rare Earths*, John Wiley & Sons, New York, **1965**.

[12] R. T. Moura Jr., A. N. Carneiro Neto, R. L. Longo, O. L. Malta, *J. Lumin.* **2016**, *170*, 420.

[13] A. N. Carneiro Neto, E. E. S. Teotonio, G. F. de Sá, H. F. Brito, J. Legendziewicz, L. D. Carlos, M. C. F. C. Felinto, P. Gawryszewska, R. T. Moura Jr., R. L. Longo, W. M. Faustino, O. L. Malta, in *Handb. Phys. Chem. Rare Earths, Vol. 56* (Eds.: J.-C.G. Bünzli, V.K. Pecharsky), Elsevier, **2019**, pp. 55–162.

[14] A. N. Carneiro Neto, R. T. Moura Jr., *Chem. Phys. Lett.* **2020**, *757*, 137884.

[15] O. L. Malta, *Chem. Phys. Lett.* **1982**, *88*, 353.

[16] O. L. Malta, *Chem. Phys. Lett.* **1982**, *87*, 27.

[17] A. N. Carneiro Neto, R. T. Moura, E. C. Aguiar, C. V Santos, M. A. F. L. B. de Medeiros, *J. Lumin.* **2018**, *201*, 451.

[18] R. T. Moura Jr., A. N. Carneiro Neto, E. C. Aguiar, C. V. Santos-Jr., E. M. de Lima, W. M. Faustino, E. E. S. Teotonio, H. F. Brito, M. C. F. C. Felinto, R. A. S. Ferreira, L. D. Carlos, R. L. Longo, O. L. Malta, *Opt. Mater. X* **2021**, *11*, 100080.

[19] W. T. Carnall, H. Crosswhite, H. M. Crosswhite, *Energy Level Structure and Transition Probabilities in the Spectra of the Trivalent Lanthanides in $LaF_3$*, Argonne, IL, United States, **1978**.

[20] G. S. Ofelt, *J. Chem. Phys.* **1963**, *38*, 2171.

[21] O. L. Malta, *J. Lumin.* **1997**, *71*, 229.

[22] E. Kasprzycka, A. N. Carneiro Neto, V. A. Trush, L. Jerzykiewicz, V. M. Amirkhanov, O. L. Malta, J. Legendziewicz, P. Gawryszewska, *J. Rare Earths* **2020**, *38*, 552.

[23] R. T. Moura, J. A. Oliveira, I. A. Santos, E. M. Lima, L. D. Carlos, E. C. Aguiar, A. N. C. Neto, *Adv. Theory Simulations* **2021**, *4*, 2000304.

[24] L. Smentek, *Phys. Rep.* **1998**, *297*, 155.

[25] S. Edvardsson, M. Klintenberg, *J. Alloys Compd.* **1998**, *275–277*, 230.

[26] A. N. Carneiro Neto, R. T. Moura, O. L. Malta, *J. Lumin.* **2019**, *210*, 342.

[27] O. L. Malta, *J. Non. Cryst. Solids* **2008**, *354*, 4770.

[28] E. Hairer, G. Wanner, in *Encycl. Appl. Comput. Math.* (Ed.: B. Engquist), Springer Berlin Heidelberg, Berlin, Heidelberg, **2015**, pp. 1213–1216.